Monthly Notices of the ROYAL ASTRONOMICAL SOCIETY

MNRAS **508,** 5217–5238 (2021) https://doi.org/10.1093/mnras/stab2914
Advance Access publication 2021 October 13

Submillimetre compactness as a critical dimension to understand the main sequence of star-forming galaxies

Annagrazia Puglisi [1]★ Emanuele Daddi [2] Francesco Valentino [3,4] Georgios Magdis,[3,4,5,6] Daizhong Liu,[7] Vasily Kokorev,[3,4] Chiara Circosta,[8] David Elbaz,[2] Frederic Bournaud,[2] Carlos Gomez-Guijarro [2] Shuowen Jin [9,10] Suzanne Madden,[2] Mark T. Sargent[11,12] and Mark Swinbank [1]

[1]*Centre for Extragalactic Astronomy, Department of Physics, Durham University, South Road, Durham DH1 3LE, UK*
[2]*CEA, Irfu, DAp, AIM, Universitè Paris-Saclay, Universitè de Paris, CNRS, F-91191 Gif-sur-Yvette, France*
[3]*Cosmic Dawn Center (DAWN), Copenhagen, Denmark*
[4]*Niels Bohr Institute, University of Copenhagen, Jagtvej 128, DK-2200 Copenhagen, Denmark*
[5]*DTU-Space, Technical University of Denmark, Elektrovej 327, DK-2800 Kgs. Lyngby, Denmark*
[6]*Institute for Astronomy, Astrophysics, Space Applications and Remote Sensing, National Observatory of Athens, GR-15236 Athens, Greece*
[7]*Max-Planck-Institut für Extraterrestrische Physik (MPE), Giessenbachstr. 1, D-85748 Garching, Germany*
[8]*Department of Physics and Astronomy, University College London, Gower Street, London WC1E 6BT, UK*
[9]*Instituto de Astrofísica de Canarias (IAC), E-38205 La Laguna, Tenerife, Spain*
[10]*Universidad de La Laguna, Dpto. Astrofísica, E-38206 La Laguna, Tenerife, Spain*
[11]*Astronomy Centre, Department of Physics and Astronomy, University of Sussex, Brighton BN1 9QH, UK*
[12]*International Space Science Institute (ISSI), Hallerstrasse 6, CH-3012 Bern, Switzerland*

Accepted 2021 October 4. Received 2021 October 4; in original form 2021 March 17

ABSTRACT

We study the interstellar medium (ISM) properties as a function of the molecular gas size for 77 infrared-selected galaxies at $z \sim 1.3$, having stellar masses $10^{9.4} \lesssim M_\star \lesssim 10^{12.0}$ M$_\odot$ and star formation rates $12 \lesssim \mathrm{SFR_{FIR}} \lesssim 1000$ M$_\odot$ yr^{-1}. Molecular gas sizes are measured on ALMA images that combine CO(2-1), CO(5-4), and underlying continuum observations, and include CO(4-3), CO(7-6) + [CI]($^3P_2 - {}^3P_1$), [CI]($^3P_1 - {}^3P_0$) observations for a subset of the sample. The $\gtrsim$46 per cent of our galaxies have a compact molecular gas reservoir, and lie below the optical discs mass–size relation. Compact galaxies on and above the main sequence have higher CO excitation and star formation efficiency than galaxies with extended molecular gas reservoirs, as traced by CO(5-4)/CO(2-1) and CO(2-1)/$L_{\mathrm{IR,\,SF}}$ ratios. Average CO + [CI] spectral line energy distributions indicate higher excitation in compacts relative to extended sources. Using CO(2-1) and dust masses as molecular gas mass tracers, and conversion factors tailored to their ISM conditions, we measure lower gas fractions in compact main-sequence galaxies compared to extended sources. We suggest that the submillimetre compactness, defined as the ratio between the molecular gas and the stellar size, is an unavoidable information to be used with the main sequence offset to describe the ISM properties of galaxies, at least above $M_\star \geq 10^{10.6}$ M$_\odot$, where our observations fully probe the main sequence scatter. Our results are consistent with mergers driving the gas in the nuclear regions, enhancing the CO excitation and star formation efficiency. Compact main-sequence galaxies are consistent with being an early post-starburst population following a merger-driven starburst episode, stressing the important role of mergers in the evolution of massive galaxies.

Key words: galaxies: evolution – galaxies: star formation – galaxies: ISM.

1 INTRODUCTION

The majority of star-forming galaxies (SFGs) are observed to follow a correlation in the stellar mass ($M_\star$) versus star formation rate (SFR) plane. In the mainstream scenario, the existence of this so-called Main Sequence (MS; Daddi et al. 2007; Elbaz et al. 2007; Noeske et al. 2007; Wuyts et al. 2011; Kashino et al. 2013; Rodighiero et al. 2014; Sargent et al. 2014; Speagle et al. 2014; Whitaker et al. 2014; Pannella et al. 2015; Renzini & Peng 2015; Schreiber et al. 2015, to mention a few) and its tight scatter (∼0.3 dex, e.g. Rodighiero et al. 2011; Sargent et al. 2012; Schreiber et al. 2015) are interpreted as evidence that star formation in most galaxies is a fairly ordered process. In particular, galaxies on the main sequence appear to be secularly evolving (Daddi et al. 2010a; Genzel et al. 2015) clumpy discs (Förster Schreiber et al. 2009) growing inside out (Nelson et al. 2012, 2016). Galaxies above the main sequence are believed to undergo a starburst mode of star formation associated with stochastic processes like major mergers (Kartaltepe et al. 2012; Hung et al. 2013; Silverman et al. 2015a, 2018a; Cibinel et al. 2019). These so-

★ E-mail: annagrazia.puglisi@durham.ac.uk

called starbursts only represent a small percentage of the star-forming galaxy population and seem to have a minor impact on the cosmic star formation history (Rodighiero et al. 2011; Schreiber et al. 2015).

On the other hand, recent studies at far-infrared (FIR) /submillimetre (sub-mm) wavelengths of galaxies at $z > 1$ are revealing a somewhat different picture. In particular, the properties of galaxies at long wavelengths seem to be poorly correlated with their main sequence position, in seeming contrast with the current interpretation of the main sequence. For example, the spatial extent of the molecular gas reservoir does not show correlations with the offset from the main sequence ($\Delta\mathrm{MS} = \mathrm{SFR/SFR_{MS}}$) or, almost equivalently, with the specific SFR (sSFR; Puglisi et al. 2019). The star formation efficiency (SFE) and molecular gas excitation are also somewhat weakly correlated with the main sequence offset (e.g. Tacconi, Genzel & Sternberg 2020, and references therein) and little difference is observed when comparing average CO spectral line energy distributions (SLEDs) of galaxies on and above the main sequence (Valentino et al. 2020). This echoes studies of the infrared spectral energy distribution (SED) showing that there is only a little difference between the far-infrared SED shape of main-sequence and starburst galaxies at $z \sim 2$ (Béthermin et al. 2015, see also Burnham et al. 2021).

In addition to an overall weak correlation between the interstellar medium (ISM) properties and the main sequence offset, it has been recently discovered that a large fraction of massive ($M_\star \gtrsim 10^{10.5}$ $\mathrm{M_\odot}$) star-forming galaxies within the main sequence have compact molecular gas reservoirs embedded in a more extended stellar structure (Tadaki et al. 2017a; Elbaz et al. 2018; Jiménez-Andrade et al. 2019, 2021; Puglisi et al. 2019; Franco et al. 2020; Tadaki et al. 2020; Gómez-Guijarro et al. 2021). These 'submillimetre compact' main-sequence galaxies have short depletion time-scales, as derived from dust-continuum measurements (Elbaz et al. 2018; Franco et al. 2020), and single-object studies show that these objects have highly excited ISM (Popping et al. 2017). These properties are consistent with the properties expected from merger-driven starbursts (Mihos & Hernquist 1996; Papadopoulos et al. 2012; Hodge et al. 2016). However, these sources display 'main sequence' levels of star-forming activity. Furthermore, ALMA observations reveal that some of these compact, star-forming cores are rotating and thus possibly discs (Tadaki et al. 2017a, b; Talia et al. 2018; Kaasinen et al. 2020). Understanding the formation mechanism of such objects is important since compact star-forming galaxies might represent a key phase in the passivization mechanisms of galaxies (Barro et al. 2013, 2014; Elbaz et al. 2018; Gómez-Guijarro et al. 2019; Puglisi et al. 2019).

Are galaxies within the main sequence uniquely associated with a secular mode of star-formation? Do we really observe two star-forming galaxy populations with different properties (extended discs in secular evolution and merger-driven starbursts) or do we rather observe a broad variety of properties in massive star-forming galaxies at $z \geq 1$? What are the mechanisms responsible for the formation of massive galaxies with a compact molecular gas reservoir within the main sequence?

In this paper, we aim to address the above questions by taking advantage of the unique coverage provided by our Atacama Large Millimeter Array (ALMA) survey presented in Valentino et al. (2020). This multicycle campaign has allowed us to obtain several carbon monoxide (CO) and neutral atomic carbon ([CI]) line detections enabling a characterization of the molecular gas excitation conditions in a statistical sample of far-infrared selected star-forming galaxies at $z \sim 1.3$. While CO scaling relations as a function of the main sequence position have been extensively discussed in Valentino et al. (2020), here we investigate the dependence of ISM properties on the spatial extent of the molecular gas reservoir. We also take advantage of the availability of different observables to estimate the gas content of our sample from multiple tracers (namely the CO(2-1) luminosity, $L'_{\mathrm{CO(2-1)}}$, and the dust mass, M_{dust}), building on the study of the ISM conditions to physically motivate the choice of the conversion factors required to convert the observables into gas masses.

The paper is organized as follows. In Section 2, we report information on the measurements that are essential for the analysis presented in this paper. These include details on the galaxy size measurements, galaxy integrated properties, and our sources classification criterion. In Section 3, we present the results on the ISM properties of the sample. We discuss these results in Section 4. Finally, we summarize the main findings of this paper in Section 5. Throughout this paper we use a Chabrier (2003) initial mass function and a standard ΛCDM cosmology ($H_0 = 70$ km s^{-1} Mpc^{-1}, $\Omega_\mathrm{m} = 0.3$, $\Omega_\Lambda = 0.7$).

2 THE SAMPLE

In this work, we study the molecular gas properties of a statistical sample of 123 galaxies at $1.1 \leq z \leq 1.7$ in the COSMOS field (Scoville et al. 2007) selected in the far-infrared to have a total infrared luminosity $L_\mathrm{IR} \gtrsim 10^{12}\,L_\odot$. These galaxies were observed with ALMA in Band 6 with an average circularized beam of ∼0.7 arcsec to detect the CO(5-4) emission (Program-ID 2015.1.00260.S, PI E. Daddi). For 75 of the 123 galaxies detected at high significance, we obtained follow-up observations of the CO(2-1) transition in ALMA Band 3 with an average circularized beam of ∼1.5 arcsec (Program-ID 2016.1.00171.S, PI E. Daddi). We also acquired CO(7-6) + [CI]($^3P_2 - {}^3P_1$) observations from a follow-up program targeting 15 of the 123 galaxies in the main program (Program-ID 2019.1.01702.S, PI F. Valentino). Finally, we complemented these observations with available CO(4-3) and [CI]($^3P_1 - {}^3P_0$) observations from an independent campaign (Program-IDs 2016.1.01040.S and 2018.1.00635.S, PI: F. Valentino) for 15 out of 123 galaxies in the primary sample. For a detailed description of the selection criteria, the full ALMA data set, the data reduction, and measurements of emission line fluxes and flux upper limits we refer the reader to Valentino et al. (2020). Here we report details of the ALMA size measurements that are used in this paper (Section 2.1). We also provide details of the measurements of stellar masses, near-infrared sizes, star formation rates, dust masses, and the intensity of the radiation field for these galaxies (Section 2.2). Finally, we present the source classification criterion adopted in our analysis, which is based on the size of the molecular gas component relative to the position of the source with respect to the optical mass–size relation (Section 2.3).

2.1 ALMA size measurements

In this work, we measure sizes from ALMA images following the methodology detailed in Puglisi et al. (2019), Valentino et al. (2020), and references therein. As already discussed in these papers, the source sizes are measured by combining all the available ALMA observations in the *uv* plane, allowing for an arbitrary re-normalization of the signal for all tracers. These include the CO(2-1), CO(4-3), CO(5-4), CO(7-6), [CI], and underlying continua. This is to maximize the accuracy of the size measurements and the sample statistics. To determine the best-fitting size and its 1σ uncertainty we compare the *uv* distance versus amplitude distribution to circular Gaussian models. Our ALMA size measurement method is exemplified in fig. 1 of Puglisi et al. (2019). The best-fitting size of each galaxy

Table 1. Summary of ALMA size measurements and CO emission lines statistics for our sample.

Quantity	N_{obj}
ALMA size	39/123
ALMA size upper limit	50/123
ALMA size or size upper limit & $M_\star$ & SFR^a_{FIR}	82/123
ALMA size or size upper limit & $M_\star$ & SFR_{FIR} & f_{AGN} <80 per cent	77/123
This work with CO(5-4)[b]	46/77
This work with CO(2-1)[c]	33/77
This work with CO(5-4) and CO(2-1)[d]	31/77

Notes. [a]We exclude 7 out of the 89 galaxies with a ALMA size or size upper limit from our analysis. Four of these galaxies have no far-infrared counterpart in the Jin et al. (2018) catalogue. Three objects are AGN and have no measurements of the stellar mass.
[b]Galaxies with CO(5-4) detections or robust upper limits (corresponding to $Flag_{CO(5-4)} \geq 0.5$ in the Valentino et al. 2020 catalogue).
[c]Galaxies with CO(2-1) detection or robust upper limits ($Flag_{CO(2-1)} \geq 0.5$).
[d]Galaxies with CO(5-4) and CO(2-1) detection or robust upper limits.

R_{eff} is defined as half of the full-width half maximum (FWHM) of the best-fitting circular Gaussian model (R_{eff} = FWHM/2). This corresponds to the half-light radius for a 2D Gaussian profile. We quantify the probability P_{unres} of each galaxy to be unresolved by comparing the best-fitting circular Gaussian χ^2 to the χ^2 for a point source. We consider a galaxy to be resolved when $P_{unres} \leqslant 10$ per cent with this threshold corresponding to 0.5 galaxies expected to be spuriously resolved in our total sample of 123 sources. Recent results have suggested that high-redshift galaxies have far-infrared profiles consistent with exponential discs (Hodge & da Cunha 2020, and references therein). However, most of these studies rely on higher resolution ALMA observations ($\lesssim$ 0.25 arcsec, e.g. Hodge et al. 2016). A circular Gaussian profile provides a good fit to galaxies in our sample given the signal-to-noise ratio (SNR) and beam of our observations. In addition, fitting an exponential profile to our data gives consistent size measurements within the errors.

We measure sizes or size upper limits for 89 out of the 123 sources observed in our ALMA program. Of these, 39 galaxies are resolved with an average size/size-error ratio of $\sim$ 10. We measure 1σ size upper limits for 50 galaxies in the sample. Finally, we cannot measure sizes for 34 sources in the sample. Of these, 18 objects lack a line detection and have uncertain emission line upper limits as a result of a poor optical redshift. In addition, 15 sources have uncertain upper limits on the CO(5-4) transition based on high-quality optical redshifts only and no continuum detection. Finally, we discard one object because of an unreliable size measurement (P_{unres} = 29 per cent) due to low SNR detections in CO and continuum. We include in Table 1 a summary of the ALMA size measurements statistics. We note that size measurements are updated with respect to those presented in Puglisi et al. (2019). This is because in this work we have included additional CO(7-6) + [CI]($^3P_2 - {}^3P_1$) and CO(4-3) and [CI]($^3P_1 - {}^3P_0$) observations in our average size estimate. This results in six additional sources with a measured size. Furthermore, this results in an average size/size-error that is $\sim$1.9 $\times$ higher than in our previous analysis (average size/size-error of $\sim$ 5.3 in Puglisi et al. 2019).

We extensively tested the reliability of our procedure to measure sizes using Monte Carlo simulations, as discussed in Puglisi et al. (2019) and Coogan et al. (2018). In brief, we created 1000 mock realizations of our data sets by perturbing the best-fitting models within the measured uncertainties in the *uv*-amplitudes plane, assuming a Gaussian distribution for the noise. We applied our procedure to measure sizes for each of these 1000 synthetic realizations. We performed this test on galaxies covering a broad range in sizes and flux SNR corresponding to that covered by our measurements (R_{eff} = 0.1−1 arcsec, flux SNR = 5−10). We find no residual systematic uncertainties in the recovered sizes within 5 per cent. For galaxies that are significantly larger than our average beam (i.e. above $\sim$1.2 arcsec), we find a small systematic uncertainties with sizes from simulations that are $\sim$10 per cent smaller than input sizes. This systematics does not depend on the SNR of the source but it seems to be rather related to the intrinsic size of the object. However, we find that the largest discrepancy is $\sim$10 per cent for the most extended sources, thus not affecting our results. We also find that the average size errorbars are consistent with the 1σ dispersion of simulated size measurement, validating the robustness of our 1σ size error bars. The robustness of the 1σ size errorbars is also indicated by the χ^2 distribution and the corresponding probability of the individual fits in the *uv* plane, which is consistent with pure noise.

2.1.1 *Potential biases in our ALMA size estimates*

Our method that combines several molecular gas tracers to measure sizes might be sensitive to different components of the ISM depending on the excitation properties of each individual galaxy. However, we verified that in all cases (but for three single notable exceptions) where multiple tracers were combined to a single size measurement, the tracers' signal versus amplitude trends agree among themselves. This suggests that for our sample there are no significant size variations between low-to-high J CO tracers and underlying dust continuum within the beam of our observations ($\sim$0.7− 1.5 arcsec, see fig. 1 in Puglisi et al. 2019). Furthermore, we find a 1:1 correlation between the ALMA sizes and the sizes of CO(5-4) or CO(4-3) and/or the underlying dust continuum ($\lambda_{rest} \sim 520-650$ μm), suggesting that ALMA sizes are mostly driven by the high-J CO transitions and/or the underlying dust continuum. When comparing CO(5-4) or CO(4-3) and 1 mm dust continuum sizes, we find that the scatter among the two independent size measurements is consistent with pure noise, leaving no space for additional systematics. Finally, for both extended and compact galaxies with robust CO(5-4) sizes (i.e. size/size error $\geq$ 3), we have verified that the CO(5-4) size is consistent within the errors with the average size obtained as the weighted average of the individual size tracers and excluding the CO(5-4). These tests justify our method to combine different molecular gas size tracers and suggests that our ALMA sizes are representative of the typical extension of the molecular gas and cold dust in our galaxies. Future ALMA observations with higher spatial resolution in multiple tracers will help us to investigate the presence of size variations as a function of the molecular gas tracer for this sample.

Another potential source of bias in our size measurements might be associated to the presence of an active galactic nucleus (AGN), since we detect AGN features in the $\sim$ 40 per cent of our sample (Valentino et al. 2020, see also Section 2.2). However, our ALMA sizes are mostly derived from the CO(5-4) emission and we do not expect a significant contribution of X-ray dominated regions (XDR) at these intermediate CO transitions (see also discussion in Section 3.1). Even when size measurements are driven by the continuum underlying the CO(5-4) emission, we expect the AGN to provide a marginal contribution to the size. In fact, our decomposition of the far-infrared SED (see below) shows a marginal AGN contribution at $\lambda_{rest} \sim$ 500 μm. This is in line with other studies showing that there is currently

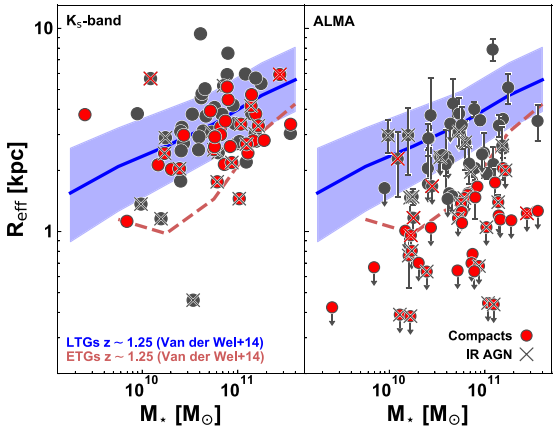

Figure 1. The left-hand panel shows the correlation between the stellar mass and the K_s-band size of our sample, roughly tracing the stellar mass size at $z \sim 1.25$. The right-hand panel shows the correlation between the stellar mass and the ALMA size. The blue line and blue shaded area indicate the van der Wel et al. (2014) relation and scatter for star-forming discs at $z \sim 1.25$. The dark-red dashed line represents the van der Wel et al. (2014) relation for early type galaxies and it is shown here as a reference. In both panels, red filled circles highlight the compact galaxies in our sample. We highlight with crosses the AGN. Sources with a strong AGN contamination to the far-infrared SED ($f_{AGN} \geq 0.8$) are highlighted with a red cross and are excluded from the rest of the analysis. In the right-hand panel, errorbars indicate the 1σ uncertainty associated with our ALMA size measurements. Down-facing arrows highlight 1σ ALMA size upper limits.

no evidence of the AGN driving the FIR continuum sizes of galaxies (e.g. Chen et al. 2020).

2.2 Galaxy integrated properties and near-infrared sizes

We obtain stellar mass measurements for the galaxies in our sample from the Laigle et al. (2016) catalogue. For the sources with a significant contribution from an AGN (see below), we repeat the fitting procedure of the UV-to-NIR photometry, following the approach detailed in Circosta et al. (2018).

As in Puglisi et al. (2019), for the 82 galaxies that have an ALMA size, a stellar mass and a star formation rate measurement (see Table 1), we measure near-infrared rest-frame sizes ($\lambda_{obs} \sim 1$ μm) from UltraVISTA K_s-band images (McCracken et al. 2012). The UltraVISTA images allow us to estimate sizes with a ~ 20 per cent accuracy (e.g. Faisst et al. 2017) and have an average seeing of ∼0.7 arcsec, which is comparable to our best ALMA beam. For consistency with the approach adopted to measure sizes on the ALMA images, we measure near-infrared sizes by fitting circular Gaussian profiles with GALFIT (Peng et al. 2010). We note that in principle, Sersic models would be more appropriate for fitting the optical/near-infrared emission of galaxies. However, our sources are only marginally resolved in the UltraVISTA observations and circular Gaussian profiles provide an adequate fit to the K_s-band images. Using an exponential disc or a Sersic profile with a free Sersic index does not significantly affect our conclusions. As already discussed in Puglisi et al. (2019), 10 out of the 82 objects considered for the analysis show a prominent point-like emission in the K_s-band imaging, likely associated with an AGN. These galaxies are not shown in the left-hand panel of Fig. 1. This does not affect our results, since K_s-band sizes are not considered for the quantitative analysis presented in this paper.

The other physical properties that are relevant for this work are the total IR luminosity L_{IR} in the rest-frame wavelength range $\lambda = 8-1000$ μm, the dust mass and the intensity of the radiation field $\langle U \rangle$. These quantities are obtained by modelling the IR photometry from the Jin et al. (2018) 'super-deblended' catalogue, and by adding the dust continuum emission observed with ALMA in the $\lambda_{obs} \in [0.8 - 3.2]$ mm wavelength range. The FIR modelling is performed by using the customized χ^2 minimization tool STARDUST (Kokorev, Magdis & Davidzon 2021)[1] and it is based on the Magdis et al. (2012) approach which uses Draine & Li (2007) dust models and a mid-infrared AGN torus component from Mullaney et al. (2011). The total infrared luminosity obtained from the fitting thus consists of a component associated with star formation ($L_{IR,\,SF}$), and one component arising from the dusty torus ($L_{IR,\,AGN}$). This allows us to estimate the fraction of the total IR luminosity associated with the dusty torus as $f_{AGN} = L_{IR,\,AGN}/L_{IR}$. Following Valentino et al. (2020), we consider that an AGN component is reliably detected when $f_{AGN} + 1\sigma_{f_{AGN}} \geqslant 20$ per cent, and we classify galaxies as AGN-dominated when $f_{AGN} \geqslant 80$ per cent. We finally measure star formation rates SFR_{FIR} from $L_{IR,\,SF}$ by using the Kennicutt (1998) calibration rescaled to a Chabrier (2003) IMF by a factor 1.7. For more details about the modelling procedure we refer the reader to Section 3.3 of Valentino et al. (2020) and references therein.

2.3 Submillimetre compactness

In Fig. 1, we show an updated version of the $M_\star$-Size plane presented in Puglisi et al. (2019). In the left-hand panel we show the K_s-band sizes, roughly tracing the size of the stellar mass distribution at $z \sim 1.25$, corresponding to the average redshift of our sample. This plot shows that nearly all the galaxies in our sample are located within the scatter of the $M_\star$–Size relation for $z \sim 1.25$ star-forming discs (or late type galaxies, LTG, van der Wel et al. 2014, blue line in Fig. 1). In the right-hand panel of Fig. 1 we show the ALMA sizes of our sources. From this plot we see that the ALMA measurements are skewed towards small size values.

We define the submillimetre compactness (or simply compactness) as:

$$C_{gas} = R_{eff,LTG}/R_{eff,ALMA}, \quad (1)$$

where $R_{eff,\,LTG}$ is the size measured from the van der Wel et al. (2014) LTG relation at the stellar mass of the galaxy, and $R_{eff,\,ALMA}$ is the ALMA size of the source. We then compute the χ^2 of the compactness distribution for the 82 galaxies with an ALMA size (or size upper limit), a measurement of the stellar mass and of the star formation rate (see equation 1 in Puglisi et al. 2019). We find that 34 per cent of the sample has an ALMA size/size upper limit consistent with the van der Wel et al. (2014) mass–size relation for star-forming discs. These galaxies have similar K_s-band and ALMA sizes. We identify these galaxies as 'extended'. Instead, 46 per cent of the galaxies have molecular gas sizes that are $\geq 1\sigma$ more compact relative to the stars as expected from the discs mass–size relation. These galaxies are highlighted in red in both panels of Fig. 1. Through the paper we will refer to these galaxies as 'compacts'. These compact sources are on average 3.3 × smaller in ALMA than in the K_s-band, on average, consistent with the measurements from our previous study (Puglisi et al. 2019). Finally, we find that 20 per cent of the sources have ALMA size upper limits within the LTG relation (black upper limits in the right-hand panel of Fig. 1). We dub those objects

[1] https://github.com/VasilyKokorev/stardust

as 'ambiguous' since we cannot place robust constraints on their compactness. We will consider these objects as a separate category through the paper.

While the stellar sizes of our sample are by and large consistent with those of typical $z \sim 1.25$ star-forming galaxies, the left-hand panel of Fig. 1 suggests that compact galaxies have slightly smaller K_s-band sizes than extended sources. To quantify this effect, we perform a two-sided Kolmogorov–Smirnov (KS) test after dividing the size inferred from the van der Wel et al. (2014) LTG relation at the stellar mass of the source by the K_s-band size. We consider only extended and compact galaxies for this test. We find median size ratios of $R_{\rm eff,LTG,Extended}/R_{\rm eff,K_s-band} = 1.03 \pm 0.38$ and $R_{\rm eff,LTG,Compacts}/R_{\rm eff,K_s-band} = 1.23 \pm 0.43$ for extended and compact galaxies, respectively. That is, compact galaxies have slightly smaller K_s-band sizes than extended sources. However, we cannot reject the null hypothesis at the ~ 10 per cent level (p-value $= 0.13$). This suggests that the K_s-band size distribution of extended and compact sources in our sample is slightly but not substantially different, as expected if compact galaxies are caught in the process of building up a dense stellar core (see also discussion in Section 4.2). Recently, Popping et al. (2021) has challenged the idea that the dust-continuum size is more compact than the stellar half-mass radius in $z \geq 1$ galaxies, due to strong dust attenuation gradients affecting H-band observations. This however corresponds to an observed-frame wavelength of $\sim$0.5 μm at $z \sim 2$. Here we use K_s-band observations (corresponding to $\sim$1 μm at $z \sim 1.25$) to sample the stellar half-mass radius and we expect negligible dust attenuation effects in this case. In fact, the emission at these wavelengths has been observed to align with the CO and radio emission even for the most obscured starbursts such as GN20 (e.g. Tan et al. 2014).

We highlight with crosses in Fig. 1 the galaxies with a reliably detected AGN contribution to the far-infrared SED. Five of the sources with an ALMA size/size upper limit have $f_{\rm AGN} \geqslant 80$ per cent (red crosses in Fig. 1). We exclude these galaxies from the analysis presented in Section 3 since we cannot derive robust SFR constraints and XDRs might contribute significantly to the CO line ratios. We find AGN signatures in 25 ± 11 per cent of the extended galaxies. Instead, we find AGN signatures in 45 ± 13 per cent of the compact sources. This suggests that compact galaxies have an enhanced AGN fraction. To test whether AGN are associated to more compact galaxies, we apply a log-rank test to the compactness distribution of galaxies with and without an AGN contribution to the far-infrared SED, accounting for the presence of compactness lower limits. We find a 94 per cent probability that the two distributions are different (p-value $= 0.06$). We note however that the AGN host population contains a larger fraction of compactness lower limits (62 per cent versus 47 per cent in galaxies without an AGN) and such lower limits are mostly associated with large compactness values. This implies that the AGN hosts' compactness distribution is not well constrained at high compactness values and the log-rank test results might be unreliable. On the other hand, this may suggest that AGN are associated with more compact galaxies for which we have stringent size upper limits. We thus conclude that our observations provide marginal evidence that AGN are more likely associated to galaxies with a compact molecular gas reservoir, similarly to that suggested by previous analyses (Elbaz et al. 2018, Puglisi et al. 2019, Lamperti et al. 2021, see also Barro et al. 2014 for optically compact star-forming galaxies). This might indicate that the mechanisms responsible for fuelling the molecular gas to the nuclear regions is also efficient in feeding the AGN.

In Fig. 2, we report the star formation rate as a function of the stellar mass for our sample. We normalize the star formation rate of each galaxy to the SFR of the main sequence at the average redshift of the sample, to account for the redshift evolution of the main sequence normalization (Sargent et al. 2012). Similar to our previous analysis, we identify as 'main sequence galaxies' sources with ΔMS$<$3.5, whereas we classify as 'off main sequence' or starbursts galaxies with ΔMS$\geq$3.5. The colour code in Fig. 2 provides information on the sources' compactness. In particular, blue circles represent galaxies with an ALMA size consistent with the LTG relation, red filled circles indicate compact sources and grey filled circles highlight ambiguous galaxies. Finally, small black dots display galaxies for which we cannot measure a size from our ALMA observations (see Table 1 and Section 2.1). We do not find a clear correlation between the compactness and the main sequence position, similarly to what reported in Puglisi et al. (2019). Galaxies with a compact molecular gas reservoir make up a significant fraction of the main sequence population above $\sim 5 \times 10^{10}$ M$_\odot$, in line with previous studies (e.g. Tadaki et al. 2017b, 2020; Elbaz et al. 2018; Puglisi et al. 2019; Franco et al. 2020). Fig. 2 also shows that, while spanning a broad range of stellar masses and star formation rate in the main sequence plane, our observations consist of 'upper main sequence' galaxies, that is, strongly star-forming galaxies above the main sequence and galaxies that probe the high specific SFR stripe of the main sequence scatter. This is a result of the far-infrared selection, which corresponds to a horizontal cut in the main sequence plane (Rodighiero et al. 2014).

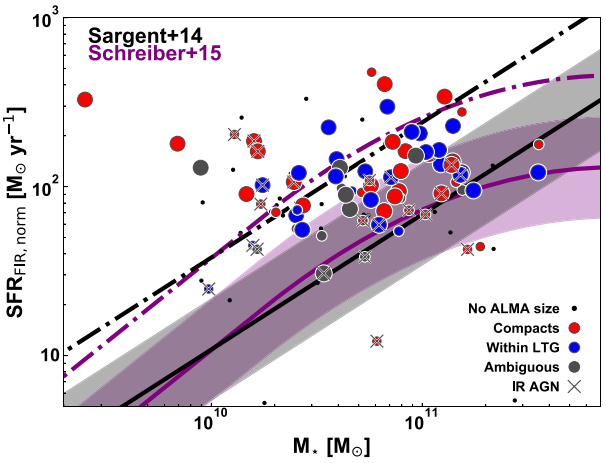

Figure 2. Star formation rate as a function of stellar mass for our sample. The solid lines indicate the main sequence locus and the shaded areas highlight the 0.3 dex main sequence scatter. The dash-dotted lines represent the 3.5× main sequence threshold above which we classify galaxies as starbursts. The black curves define these loci according to the parametrization of Sargent et al. (2014) at $z \sim 1.25$. The violet curves correspond to the Schreiber et al. (2015) parametrization at $z \sim 1.25$. The blue and red circles highlight extended and compact galaxies respectively. The grey circles indicate ambiguous sources. Larger symbols indicate galaxies with CO(5-4) or CO(2-1) observations that are considered for the analysis presented in Section 3. We highlight with crosses the AGN. The black dots indicate galaxies without ALMA size measurements.

3 RESULTS

In the following, we study the molecular gas properties of our sample as a function of the compactness and the main sequence offset. For consistency with our previous studies, we quantify the main sequence offset using the main sequence parametrization from Sargent et al. (2014). We also checked that using the widely adopted

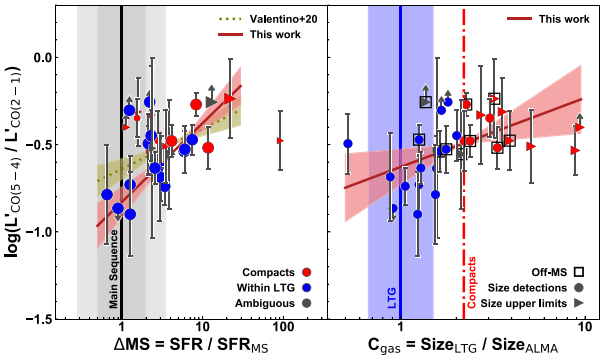

Figure 3. R_{52} as a function of the main sequence offset (left-hand panel) and the compactness (right-hand panel). In the left-hand panel, the black line, dark grey, and grey shaded areas highlight the main sequence position, the 1σ scatter and the $\pm 3.5 \times$ ΔMS region, respectively. The green dotted line and shaded area indicate the R_{52}-ΔMS trend and 1σ confidence interval fromValentino et al. (2020). The dark red solid line and shaded area indicate the R_{52}-ΔMS trend and 1σ confidence interval obtained after excluding compact and ambiguous main-sequence galaxies from the fit. The data points considered for this fit are highlighted with larger symbols. In the right-hand panel, the blue area shows the LTG relation and scatter at the average stellar mass of our sample. The red dash-dotted line marks the threshold above which galaxies are classified as compacts. The dark red solid line and shaded area indicate the R_{52}-$C_{\rm gas}$ trend and 1σ confidence interval. The blue circles indicate extended ALMA galaxies. The red symbols highlight the compacts. The grey symbols represent ambiguous sources. Right facing triangles indicate compactness upper limits. In the right-hand panel we highlight with open squares galaxies with ΔMS $\geq$3.5. Errorbars on R_{52} are obtained by propagating the 1σ uncertainty associated to the CO(5-4) and CO(2-1) flux measurements. The typical 1σ error on ΔMS is 0.2 dex accounting for observational uncertainties on SFR and $M_\star$. The 1σ typical error on $C_{\rm gas}$ is 0.2 dex considering observational uncertainties on $R_{\rm eff,\ ALMA}$.

parametrization from Schreiber et al. (2015), which accounts for the bending of the main sequence at high stellar masses, does not affect the main sequence position of our sample. For this analysis, unless stated otherwise, we consider only galaxies with reliable CO fluxes or robust CO flux upper limits. The latter corresponds to reliable upper limits on the line flux, given the presence of alternative sub-mm lines confirming the redshift obtained from the ALMA spectra ($z_{\rm spec,\ sub\text{-}mm}$). We then compute the $L'_{\rm CO}$ luminosities using the flux and $z_{\rm spec,\ sub\text{-}mm}$ measurements from our public catalogue (Valentino et al. 2020).

3.1 Gas excitation

3.1.1 The $L'_{\rm CO(5-4)}/L'_{\rm CO(2-1)}$ ratio

In Fig. 3, we show the $R_{52} = L'_{\rm CO(5-4)}/L'_{\rm CO(2-1)}$ ratio as a function of ΔMS (left-hand panel) and $C_{\rm gas}$ (right-hand panel). The R_{52} ratio is a proxy for the CO excitation and this plot allows us to infer the excitation properties of each galaxy as a function of their structural and star formation rate properties.

The left-hand panel of Fig. 3 shows that there is a substantial number of compact galaxies within a factor of $\pm$3.5 around the main sequence. These compact galaxies within the main sequence have an enhanced R_{52} ratio with respect to their extended counterparts. The R_{52} ratio of compact main-sequence galaxies is instead similar to that of galaxies above the main sequence. This plot suggests that compact and ambiguous galaxies within the main sequence contribute to the scatter observed in the R_{52}–ΔMS relation reported in Valentino et al. (2020) and obtained using the same sample considered in this work (green dotted line in the left-hand panel of Fig. 3). To quantify the contribution of these galaxies to the scatter observed in the Valentino et al. (2020) relation, we fit R_{52} as a function of ΔMS excluding compact and ambiguous galaxies with ΔMS $\leq\pm$3.5. We also exclude the strongest outlier above the main sequence, for consistency with our previous analysis. We apply a Bayesian regression analysis in the log–log space using the Python version of the LINMIX_ERR.PRO package (Kelly 2007). The results of this fit are listed in Table 2. The best-fitting line is shown as a dark red solid line in the left-hand panel of Fig. 3. The slope is $\beta = 0.45 \pm 0.14$ and this is $\sim$2 $\times$ steeper at $\sim 1.3\sigma$ than the trend reported in Valentino et al. (2020) when considering all galaxies regardless of their compactness. The intrinsic scatter of the best-fitting relation ($\sigma_{\rm int} = 0.11 \pm 0.03$) is slightly reduced. Finally, the correlation between R_{52} and ΔMS strengthens when excluding compact and ambiguous main sequence galaxies from the fit. This suggests that the presence of compact/ambiguous galaxies (i.e. non-typical discs) within the main sequence blurs the correlation between R_{52} and ΔMS. We note however that the compactness classification criterion applied in this paper reduces the source statistics with respect to the analysis presented in Valentino et al. (2020).

The right-hand panel of Fig. 3 shows a trend of increasing R_{52} as a function of the compactness. To quantify the correlation between R_{52} and $C_{\rm gas}$ we apply a Bayesian regression analysis in the log–log space similarly to that described above. The results of this fit are listed in Table 2. We show the best-fitting line as a red line in the right-hand panel of Fig. 3. The slope of the $C_{\rm gas}$–R_{52} trend is $\beta = 0.40 \pm 0.30$ and this is similar to the slope of the ΔMS–R_{52} best-fitting relation discussed above. However, the slope of the $C_{\rm gas}$–R_{52} relation is poorly constrained. The $C_{\rm gas}$–R_{52} correlation index is smaller than the R_{52}–ΔMS correlation index obtained above. We note however that our data only allow us to probe a limited compactness range due to an average $\sim$1 arcsec beam. Observations with a smaller beam would be required to probe a wider range of sizes and explore in more details the relation between R_{52} and the compactness.

3.1.2 Average CO spectral line energy distributions as a function of the compactness

In the previous section, we used the R_{52} ratio to study the CO excitation as a function of the main sequence offset and the compactness in individual galaxies in our sample. However, CO(4-3) and CO(7-6) observations available for a subset of our sources (see Tables 3 and 4) allow us to construct average CO spectral line energy distributions (SLEDs) for the three classes of sources identified in Section 2.3. We thus construct average CO SLEDs for the galaxies that have CO(2-1) and CO(5-4) emission line detections/upper limits, and a measurement of the compactness. We split those sources into different subsamples according to their compactness and main sequence position and we compute average $L'_{\rm CO}$ luminosities using a survival analysis technique to account for the presence of upper limits (Kaplan & Meier 1958). We report in Tables 3 and 4 the average CO luminosities of each subsample along with the detection statistics for each transition. We then convert the average $L'_{\rm CO}$ luminosities into CO fluxes at $z \sim 1.25$, corresponding to the average redshift of the sample. Errors on the average $L'_{\rm CO}$ luminosities and average $I_{\rm CO}$ fluxes quoted throughout this section correspond to the interquartile range from the distribution of individual measurements in each subsample.

In Fig. 4, we show the average SLEDs for extended, ambiguous, and compact galaxies in our sample. Here we include as a reference

Table 2. Scaling relations between CO properties, main sequence offset, and compactness.

Relation x, y	Slope β	Intercept α	Intrinsic scatter $\sigma_{\rm int}$	Correlation ρ	$N_{\rm det}$, $N^a_{\rm lim}$
		Distance from the main sequence			
ΔMS, $R^{\dagger}_{52}$	0.45 ± 0.14	-0.83 ± 0.09	0.11 ± 0.03	0.78	19,4
ΔMS, $L'_{\rm CO(2-1)}/L^{\dagger}_{\rm IR,SF}$	-0.42 ± 0.14	-1.73 ± 0.09	0.22 ± 0.04	-0.58	21,4
		Compactness			
$C_{\rm gas}$, R_{52}	0.40 ± 0.30	-0.63 ± 0.10	0.10 ± 0.04	0.57	25,5
$C_{\rm gas}$, $L'_{\rm CO(2-1)}/L_{\rm IR,SF}$	-0.56 ± 0.31	-1.85 ± 0.11	0.23 ± 0.05	-0.5	29,4
$C_{\rm gas}$, $\mu_{\rm gas,\ dust}$	-1.44 ± 0.5	0.05 ± 0.17	0.44 ± 0.06	-0.53	69,-

Notes. In this table we quote the mean of the best-fitting parameters from LINMIX and corresponding 1σ error bars.
†Excluding compacts and ambiguous within the main sequence.
^{a}Number of sources with CO line ratio measurements and upper/lower limits used to infer the relations presented in this table. We note that the LINMIX_ERR.PRO package does not allow us to account for the presence of upper and lower limits at the same time. Therefore, the best-fitting parameters for the ΔMS–R_{52} and $C_{\rm gas}$–R_{52} relation reported here are derived considering R_{52} detections only. We have however tested that including R_{52} detections and upper limits or R_{52} detections and lower limits we obtain fully consistent results. This is analogous to what we have performed in our previous analysis (Valentino et al. 2020).

Table 3. Average CO and [CI] luminosities and detection statistics for galaxies classified as a function of their compactness. The $L^{'}$ luminosities are expressed in 10^{10} K km s^{-1} pc^2. The average I fluxes in Fig. 4 are expressed in Jy km s^{-1} and are computed from $L^{'}$ luminosities by adopting $z = 1.25$.

Transition	$N_{\rm det}$, $N_{\rm up}$	Mean	Median
	Within LTG		
$L'_{\rm CO(2-1)}$	13, 2	2.13 ± 0.32^{a}	$1.70^{+0.97}_{-0.11}$
$L'_{\rm CO(4-3)}$	4, 0	0.66 ± 0.07	$0.59^{+0.12}_{-0.12}$
$L'_{\rm CO(5-4)}$	14, 1	0.54 ± 0.07^{a}	$0.46^{+0.21}_{-0.14}$
$L'_{\rm CO(7-6)}$	5, 0	0.20 ± 0.04	$0.18^{+0.03}_{-0.09}$
$L'_{\rm CI[1-0]}$	6, 0	0.41 ± 0.06	$0.368^{+0.07}_{-0.12}$
$L'_{\rm CI[2-1]}$	5, 0	0.18 ± 0.02	$0.19^{+0.01}_{-0.08}$
	Ambiguous		
Transition	$N_{\rm det}$, $N_{\rm up}$	Mean	Median
$L'_{\rm CO(2-1)}$	2, 2	0.66 ± 0.26^{a}	–
$L'_{\rm CO(4-3)}$	1, 0	0.72	–
$L'_{\rm CO(5-4)}$	3, 1	0.30 ± 0.06^{a}	$0.22^{+0.19}_{-0.08}$
$L'_{\rm CO(7-6)}$	–	–	–
$L'_{\rm CI[1-0]}$	0, 1	0.07	–
$L'_{\rm CI[2-1]}$	–	–	–
	Compacts		
Transition	$N_{\rm det}$, $N_{\rm up}$	Mean	Median
$L'_{\rm CO(2-1)}$	11, 1	1.67 ± 0.26^{a}	$1.49^{+0.61}_{-0.60}$
$L'_{\rm CO(4-3)}$	–	–	–
$L'_{\rm CO(5-4)}$	12, 0	0.67 ± 0.09	$0.54^{+0.43}_{-0.12}$
$L'_{\rm CO(7-6)}$	4, 0	0.26 ± 0.05	$0.19^{+0.09}_{-0.04}$
$L'_{\rm CI[1-0]}$	2, 1	0.29 ± 0.10^{a}	–
$L'_{\rm CI[2-1]}$	4, 0	0.26 ± 0.04	$0.25^{+0.001}_{-0.1}$

Note.^{a}Formally biased mean value, as the first upper limit was turned into a detection for the calculation of the KM estimator (Kaplan & Meier 1958).

Table 4. As in Table 3 but for extended and compact galaxies on and above the main sequence.

Transition	$N_{\rm det}$, $N_{\rm up}$	Mean	Median
	Within LTG, on MS (ΔMS ≤ 3.5)		
$L'_{\rm CO(2-1)}$	10, 2	2.22 ± 0.39^{a}	$1.70^{+1.88}_{-0.22}$
$L'_{\rm CO(4-3)}$	4, 0	0.66 ± 0.07	$0.59^{+0.12}_{-0.12}$
$L'_{\rm CO(5-4)}$	11, 1	0.54 ± 0.09^{a}	$0.39^{+0.44}_{-0.09}$
$L'_{\rm CO(7-6)}$	3, 0	0.19 ± 0.06	–
$L'_{\rm CI[1-0]}$	6, 0	0.41 ± 0.06	$0.37^{+0.07}_{-0.12}$
$L'_{\rm CI[2-1]}$	3, 0	0.17 ± 0.04	–
	Within LTG, off MS (ΔMS >3.5)		
Transition	$N_{\rm det}$, $N_{\rm up}$	Mean	Median
$L'_{\rm CO(2-1)}$	3, 0	1.80 ± 0.06	–
$L'_{\rm CO(4-3)}$	–	–	–
$L'_{\rm CO(5-4)}$	3, 0	0.56 ± 0.03	–
$L'_{\rm CO(7-6)}$	2, 0	0.20 ± 0.01	–
$L'_{\rm CI[1-0]}$	–	–	–
$L'_{\rm CI[2-1]}$	2, 0	0.19 ± 0.01	–
	Compacts, on MS (ΔMS ≤ 3.5)		
Transition	$N_{\rm det}$, $N_{\rm up}$	Mean	Median
$L'_{\rm CO(2-1)}$	6, 1	1.22 ± 0.21^{a}	$1.04^{+0.49}_{-0.30}$
$L'_{\rm CO(4-3)}$	–	–	–
$L'_{\rm CO(5-4)}$	7, 0	0.52 ± 0.08	$0.43^{+0.11}_{-0.08}$
$L'_{\rm CO(7-6)}$	2, 0	0.17 ± 0.01	–
$L'_{\rm CI[1-0]}$	1, 1	0.19 ± 0.09^{a}	–
$L'_{\rm CI[2-1]}$	2, 0	0.20 ± 0.03	–
	Compacts, off MS ΔMS >3.5)		
Transition	$N_{\rm det}$, $N_{\rm up}$	Mean	Median
$L'_{\rm CO(2-1)}$	5, 0	2.30 ± 0.41	$2.09^{+0.66}_{-0.98}$
$L'_{\rm CO(4-3)}$	–	–	–
$L'_{\rm CO(5-4)}$	5, 0	0.89 ± 0.14	$0.77^{+0.36}_{-0.26}$
$L'_{\rm CO(7-6)}$	2, 0	0.35 ± 0.05	–
$L'_{\rm CI[1-0]}$	1, 0	0.48	–
$L'_{\rm CI[2-1]}$	2, 0	0.31 ± 0.05	–

the average CO SLEDs from Valentino et al. (2020), which uses the same sample considered in this work but classifies galaxies according to their main sequence offset. A comparison with other galaxy types and QSO SLEDs for this sample has already been performed in Valentino et al. (2020) and we refer the reader to this paper for more details in this regard (see in particular their Section 4.4). Here we find that the CO SLED of extended galaxies closely resembles that of main sequence galaxies at $z \sim 1.25$. The CO excitation ladder of compact galaxies is consistent with that of the strongest main-sequence outliers, defined as galaxies with ΔMS $\geq$7. Likewise, ambiguous galaxies have a CO SLED similar to that of strong starbursts, possibly suggesting that these sources are more compact than indicated by their loose ALMA size upper limits. We

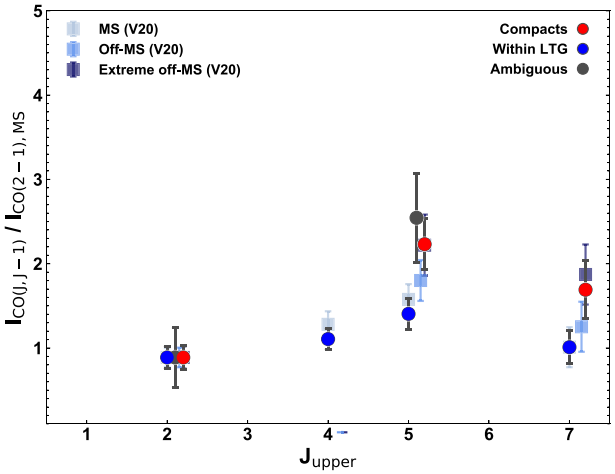

Figure 4. Average CO SLED of extended, ambiguous, and compact galaxies (blue, grey, and red circles, respectively). As a reference we show the average SLEDs of main sequence (ΔMS$\leq$3.5), off main sequence (ΔMS$\geq$3.5) and extreme off main sequence (ΔMS$\geq$7) galaxies from Valentino et al. (2020) with light blue, blue, and dark blue shaded squares, respectively. We normalize the data points to the mean CO(2-1) flux + 1σ flux error of $z \sim 1.25$ main sequence galaxies.

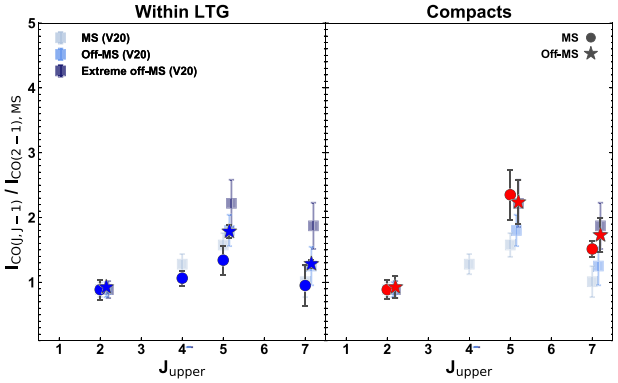

Figure 5. Average CO SLED of extended (left-hand panel) and compact (right-hand panel) galaxies in our sample, split according to their main sequence position. In both panels, circles indicate the average SLED of galaxies with ΔMS <3.5 and stars show the SLED for galaxies with ΔMS $\geq$3.5.

note however that the CO lines statistics are significantly limited for this class of objects (see Table 3) and future observations would be required to better understand their nature. Given the limited statistics, we do not investigate any further the CO SLED properties of the ambiguous galaxies subsample.

One might expect that the different excitation properties of extended and compact galaxies might be due to a higher AGN contribution to the latter sample, since we have shown in Section 2.3 that compact galaxies have a marginally higher AGN fraction. However, we have explored the contribution of AGN to the observed CO line ratios and to the average CO SLEDs in our sample in a dedicated study (Valentino et al. 2021). This analysis shows that there are no statistically significant differences between the R_{52} ratios and the average CO SLEDs of galaxies with and without an AGN when considering galaxies with $f_{AGN} < 80$ per cent as in this work. Furthermore, the authors find no differences in the CO(7-6)/CO(2-1) ratios of galaxies with and without an AGN. This suggests that the differences seen in the CO excitation of extended and compact galaxies are driven by the different star formation properties of the two subsamples up to CO(7-6). These findings are consistent with other studies showing that the R_{52} ratios does not correlate with the AGN fraction (Liu et al. 2021). This is also in agreement with other studies showing that there are not statistically significant differences in the CO SLED of star-forming versus AGN-dominated galaxies, at least when considering low-to-mid-J CO transition (Brusa et al. 2018; Kirkpatrick et al. 2019; Boogaard et al. 2020). This supports the idea that the low-to-mid J CO emission is dominated by processes associated to star formation.

To investigate additional dependencies of the CO SLED shape on the main sequence offset, we split extended and compacts between on- and off-main sequence sources. For this exercise, we classify as on-main sequence galaxies with ΔMS<3.5 and off-main sequence galaxies with ΔMS$\geq$3.5. We show in Fig. 5 the average CO SLEDs of these sources. Extended galaxies within and above the main sequence have slightly different CO SLEDs. In particular, extended main-sequence galaxies seem slightly less excited than extended galaxies above it. We also note that the CO SLED of main sequence galaxies in the Valentino et al. (2020) analysis (light blue squares in Fig. 5) is intermediate between that of extended galaxies on and above the main sequence presented here. This suggests that main sequence galaxies may not represent a homogeneous population, similarly to that reported in Section 3.1.1. On the other hand, compact galaxies on and above the main sequence have remarkably similar CO SLEDs and these are consistent with that of the most extreme main-sequence outliers (dark blue squares in Fig. 5).

Figs 4 and 5 suggest that the CO excitation increases as a function of the source compactness. This dependence seems more significant than the variations of the CO excitation with the main sequence offset. To quantify this effect, we compute line ratios as a function of the compactness and the main sequence position (see Table 5). The average R_{52} and R_{72} ratios of compact galaxies are 1.6 $\times$ and 1.8 $\times$ higher than that of extended galaxies. Instead, compact galaxies have R_{52} and R_{72} ratios that are 1.8 $\times$ higher than in extended galaxies within the main sequence. Focusing on the off-main sequence population, compact galaxies are 1.3$\times$ and 1.4$\times$ more excited in CO(5-4) and CO(7-6) than their few extended counterparts. The R_{52} and R_{72} excitation ratios of compact galaxies on and above the main sequence are consistent with each other within the error bars, suggesting homogeneous CO excitation properties. On the other hand, we find marginal evidence for variations in the excitation ratios of extended sources as a function of the MS position. In particular, extended galaxies above the main sequence have R_{52} and R_{72} ratios that are 1.3$\times$ and 1.4$\times$ higher than in extended main sequence galaxies. This might indicate an evolutionary trend with extended galaxies above the main sequence being merging pairs in an early stage of the interaction. Alternatively, this might suggest that extended off-main sequence galaxies are gas-rich starbursting discs with enhanced star formation rates after anomalous gas accretion episodes (e.g. Scoville et al. 2016). Observations with increased spatial resolution will allow us to identify any unresolved merger pairs among extended galaxies above the main sequence.

These results suggest that main sequence sources do not represent a homogeneous population in terms of CO excitation properties, as also anticipated in Valentino et al. (2020). Thus, adopting a CO excitation correction that is based on the main sequence position of a galaxy would introduce significant uncertainties in, e.g. the derived CO fluxes due to the presence of a variety of CO SLEDs within the main sequence. This is indicated by the measured R_{52} ratios within the main sequence ranging from a minimum value of

Table 5. Average line luminosities ratios for galaxies at $z \sim 1.25$. The ratios and their 1σ uncertainties are computed analytically based on the mean L' luminosities in Tables 3 and 4.

Transition	Within LTG	Within LTG, on MS	Within LTG, above MS	Compacts	Compacts, on MS	Compacts, above MS
R_{42}	0.31 ± 0.06	0.30 ± 0.03	–	–	–	–
R_{52}	0.25 ± 0.05	0.24 ± 0.06	0.31 ± 0.02	0.40 ± 0.08	0.43 ± 0.10	0.39 ± 0.09
R_{72}	0.09 ± 0.02	0.08 ± 0.03	0.11 ± 0.01	0.16 ± 0.04	0.14 ± 0.02	0.15 ± 0.04

$R_{52,\,\mathrm{MS,\,min}} = 0.13 \pm 0.03$ to a maximum value of $R_{52,\,\mathrm{MS,\,max}} \gtrsim 0.55$. The submillimetre compactness classification, on the other hand, allows us to select galaxies with more homogeneous CO excitation properties, in agreement with the results from individual CO line ratios discussed in the previous section. Given the relatively small number of sources, we caution the reader that the observed variations should be taken as indicative. Future studies with larger statistics will allow us to better investigate variations of the CO SLED with the main sequence offset and the galaxy compactness.

3.1.3 *Large velocity gradient modelling*

To better understand the CO excitation properties of our galaxies, we apply a Large Velocity Gradient (LVG) modelling to the observed average SLEDs of our sample. We report few details about the modelling below and we refer the reader to Daddi et al. (2015) and Liu et al. (2015b) for a detailed description of the approach. We create a grid of LVG models using the RADEX tool (van der Tak et al. 2007). As RADEX requires the input of the $[\mathrm{CO/H_2}]$ abundance ratio, turbulence Doppler line width (δV) and a $\mathrm{H_2}$ column density ($N_{\mathrm{H_2}}$) separately, we set them to $[\mathrm{CO/H_2}] = 5 \times 10^{-5}$, $\delta \mathrm{V} = 50\,\mathrm{km\,s^{-1}}$ and $N_{\mathrm{H_2}}/n_{\mathrm{H_2}} = 10$ pc. This implies a velocity gradient of 5 $\mathrm{km\,s^{-1}\,pc^{-1}}$, consistent with or in the range of the findings for Galactic centre or relatively dense and warm clouds (Goldreich & Kwan 1974; Dahmen et al. 1998; Ao et al. 2013) and extragalactic molecular gas in local actively star-forming galaxies (Curran et al. 2001; Weiß et al. 2001; Weiß, Walter & Scoville 2005; Zhang et al. 2014) and high-redshift galaxies (Weiß et al. 2007; Dannerbauer et al. 2009). We note that these quantities are degenerate. Given that the SLEDs of our galaxies are not fully sampled, leaving the velocity gradient or the abundance free to vary would result in much larger uncertainties. Due to the degeneracy of the models, a different set of assumed values of velocity gradients or abundances will lead to no difference in determining the $n_{\mathrm{H_2}}$ and T_{kin}, but could systematically bias the optical depth, the filling factor and hence the total mass from LVG. Thus in this work we only use the LVG fitting to infer $n_{\mathrm{H_2}}$ and T_{kin}. To better constrain the fit, we include the [C I] transitions available for a subset of the sample (see Tables 3 and 4). This allows us to provide additional information to the total gas content, since this transition correlates with the total infrared luminosity similar to low-J CO transitions (Valentino et al. 2018). Here we assume that the neutral atomic carbon is co-spatial with CO and a fixed $[\mathrm{C^0/H_2}] = 3 \times 10^{-5}$ abundance (Weiß et al. 2003; Papadopoulos, Thi & Viti 2004).

We compute the grid at the median redshift of the sample spanning a density and temperature range of $n(\mathrm{H_2}) = 10^2 - 10^6$ $\mathrm{cm^{-3}}$ and $T_{\mathrm{kin}} = 5 - 300$ K, including the appropriate value of the temperature of the cosmic microwave background. We derive the best-fitting model, the best-fitting parameters and their 1σ uncertainties using a customized χ^2 minimization algorithm, optimized for the exploration of highly multidimensional spaces (MICHI2[2]; Liu et al. 2021). We iteratively sampled the χ^2 distribution 15 000 and 10 000 times for the single and two components modelling, respectively (see below), randomizing the parameters within normal distributions centred on the minimal χ^2 derived from the previous iteration, artificially inflating their widths.

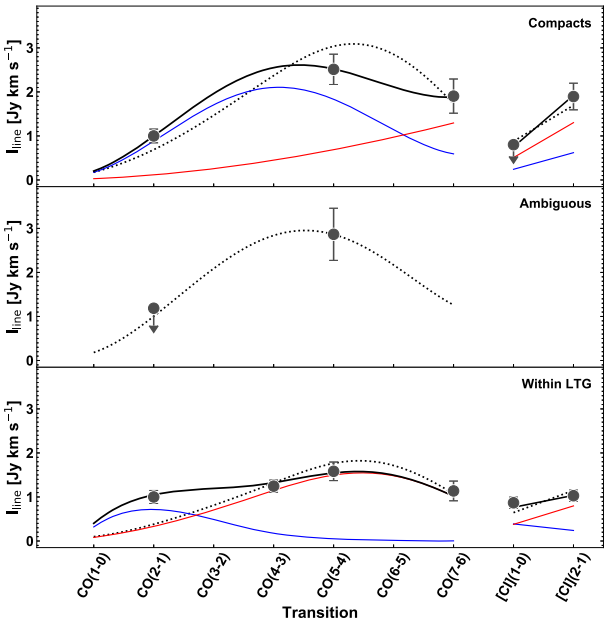

Figure 6. LVG modelling of the observed CO + [CI] SLEDs for galaxies within the LTG relation (bottom panel), galaxies with a size upper limit within the LTG relation (ambiguous, central panel), and compact galaxies (top panel). The filled symbols show the mean fluxes while arrows indicate 3σ upper limits. The dotted black line shows the best-fitting model with a single component. The blue and red lines show the low- and high-excitation components of the two components LVG modelling, with the black solid line indicating their sum.

A single component model can only reproduce the CO SLED of ambiguous galaxies (see central panel in Fig. 6), likely because of the limited amount of information available. Both the density and temperature are poorly constrained for this subsample. Instead, Fig. 6 shows that a single component model does not properly fit the observed CO SLEDs of the rest of the subsamples. In particular, it significantly underestimates the CO(2-1) emission of both extended and compact galaxies (bottom and top panels in Fig. 6) while overestimating their CO(5-4) emission. Similar trends are observed when we further distinguish between galaxies based on their main sequence position (see Fig. 7). This is consistent with previous studies (e.g. Riechers et al. 2011; Hodge et al. 2013; Kamenetzky et al. 2014; Zhang et al. 2014; Daddi et al. 2015; Liu et al. 2015b; Kamenetzky, Rangwala & Glenn 2017).

We thus perform a two components LVG modelling, by assuming the presence of a diffuse and dense gas phase with $n(\mathrm{H_2}, \mathrm{low}) < n(\mathrm{H_2}, \mathrm{high})$. This allows us to better constrain $n(\mathrm{H_2})$, but does not allow us to place robust constraints on T_{kin}. We report the best-fitting parameters

[2]https://ascl.net/code/v/2533

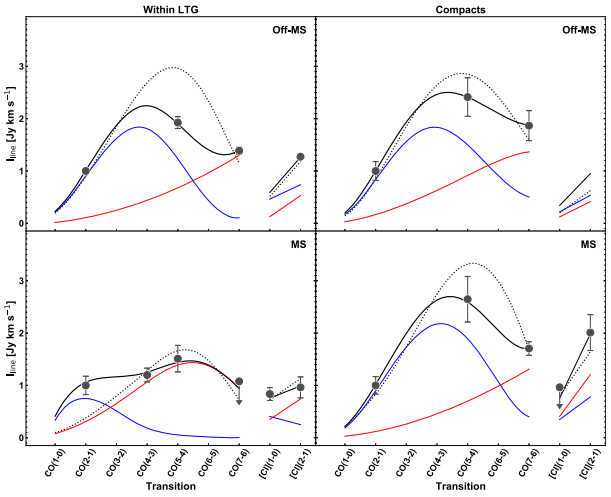

Figure 7. LVG fit to the observed CO + [CI] SLEDs for extended (left-hand panel) and compact (right-hand panel) galaxies in our sample, split according to their main sequence position as in Fig. 5. Colour code is analogous to Fig. 6.

from the two components modelling in Table 6. We find that all galaxies are characterized by low- and high- density gas components, with compacts having marginally higher gas densities than extended sources ($n_{\rm H_2,low} \sim 10^2 - 10^4$ cm^{-3} and $n_{\rm H_2,high} \sim 10^4 - 10^6$ for the compacts, while $n_{\rm H_2,low} \sim 10^2 - 10^3$ cm^{-3} and $n_{\rm H_2,high} \sim 10^3 - 10^4$ cm^{-3} for the extended sample, see also Table 6). We also find that ~ 40 per cent of the total molecular gas mass of extended galaxies is in the dense component. The best-fitting high-density component for the compacts is rising at high J (see top panel in Fig. 6 and right-hand panels in Fig. 7). While we caution that we have no constraints on the CO SLEDs of our sources beyond $J = 7$ and the LVG best-fitting models are highly extrapolated for higher-J CO observations, this might suggest that the average CO SLED of this population is dominated by an excited and dense gas component, similarly to what is observed in the starburst-dominated local ULIRG Arp220 (Rangwala et al. 2011) and high-redshift SMGs (Yang et al. 2017; Cañameras et al. 2018; Birkin et al. 2021). On the other hand, it is unlikely that the CO SLED of our sources up to $J = 7$ is dominated by the AGN component. In fact, even in local QSOs such as Mrk 231, the CO excitation up to $J = 8$ can be explained by heating from star formation (van der Werf et al. 2010). We also note that our best-fitting LVG models seem to suggest a somewhat different behaviour for compact galaxies on and above the main sequence (see top and bottom right-hand panels in Fig. 7). However, this is likely due to the lack of constraints on the [C I] transitions for the off main-sequence compact population, since the shape of the observed CO SLEDs is nearly identical for the two classes of galaxies up to $J = 7$ (see right-hand panel in Fig. 5). The best-fitting parameters derived from the LVG analysis of the two subsamples are consistent within the uncertainties (see Table 6).

3.2 Star formation efficiency and depletion time

In the left-hand panel of Fig. 8 we show the $L'_{\rm CO(2-1)}$ luminosity as a function of $L_{\rm IR,\,SF}$ for the galaxies with CO(2-1) detections or upper limits in our sample. This is the so-called integrated Schmidt–Kennicutt plane and it allows us to study the relation between the molecular gas content and star formation rate, hence the nature of star formation in our sample (e.g. Daddi et al. 2010b; Sargent et al. 2014). Extended galaxies are on average close to the region of discs (Sargent et al. 2014, solid black line in Fig. 8). Compacts seem to be globally shifted towards the dash-dotted line in Fig. 8, defining the 'strong starbursts' (ΔMS $\gtrsim$ 15) locus in the $L'_{\rm CO(2-1)}$ versus $L'_{\rm IR,SF}$ plane according to the Sargent et al. (2014) model (see also Solomon & Vanden Bout 2005; Greve et al. 2005). In the right-hand panel of Fig. 8 we show the $L'_{\rm CO(1-0)}$ luminosity as a function of $L_{\rm IR,\,SF}$. To construct this plot, we use CO(2-1) fluxes, where available. To increase the statistics, we also include galaxies without CO(2-1) observations by converting their CO(5-4) flux to CO(2-1) using a R_{52} that is appropriate for their average SLED shape (see Section 3.1 and Table 5). We do not include galaxies in the ambiguous sample because their average excitation properties are poorly constrained. We stress however that mid/high-J CO transitions sample the denser phase of the molecular gas associated with star formation (Daddi et al. 2015; Liu et al. 2015b; Valentino et al. 2020) and should not be used as a proxy of the molecular gas mass when no direct constraints on the excitation correction are available. We finally convert the CO(2-1) flux to $L'_{\rm CO(1-0)}$ using $R_{21} = 0.85$, which is the average CO(2-1)-to-CO(1-0) ratio measured in star-forming galaxies at high redshift (Bothwell et al. 2013; Daddi et al. 2015; Boogaard et al. 2020). Using an homogeneous excitation correction for the CO(2-1) luminosity is a conservative choice since galaxies with an enhanced R_{52} ratio are expected to also show an enhanced R_{21} ratio (see e.g. Daddi et al. 2015). Implementing a differential excitation correction would thus exacerbate the tension between the extended and compact populations. The right-hand panel of Fig. 8 shows that the offset between compacts and extended galaxies increases when accounting for differences in the excitation properties of the two populations.

To quantify the separation between extended and compact galaxies in the $L'_{\rm CO(1-0)}$ versus $L_{\rm IR,\,SF}$ plane, we fit the two populations independently using a linear function in the log–log space and accounting for upper limits as described in Section 3.1. We then consider only the best-fitting solutions yielding a slope $\beta = 0.81 \pm 0.03$, i.e. consistent with the value reported in Sargent et al. (2014). We find that extended galaxies have a best-fitting normalization value of 0.46 ± 0.22 which is consistent with the Sargent et al. (2014) value for discs. We find a best-fitting normalization of 0.18 ± 0.22 for the compacts. This corresponds to a $\sim$2 $\times$ offset between compact and extended galaxies. This value is intermediate between the factor of 3 $\times$ offset from Sargent et al. (2014) and the 1.7 $\times$ offset reported by Silverman et al. (2015b) for $z \sim 1.5$ starbursts. We obtain consistent results when considering the $L'_{\rm CO(2-1)}$ luminosity in the left-hand panel of Fig. 8. To quantify the significance of the offset between compact and extended galaxies, we compare the distributions of the two subsamples after subtracting the $\beta \times L_{\rm IR,\,SF}$ trend from the observed $L'_{\rm CO(1-0)}$ luminosity. We perform a log-rank test accounting for the presence of upper limits as described in the previous section. We find a 99.4 per cent probability that the distributions of compacts and extended galaxies in the right-hand panel of Fig. 8 are different (p-value = 0.0058).

The low-J CO transitions are proxies for the molecular gas content (Carilli & Walter 2013; Tacconi et al. 2020) while $L_{\rm IR,\,SF}$ quantifies the star-forming activity of a galaxy. Therefore, Fig. 8 suggest that compact galaxies in our sample have an enhanced star formation efficiency (SFE = $M_{\rm gas}$/SFR) and a lower depletion time ($\tau_{\rm depl}$ = SFR/$M_{\rm gas}$ = 1/SFE) than extended galaxies. It also appears that extended and compacts off-main sequence galaxies (open black squares in Fig. 8) preferentially occupy the region with high $L_{\rm IR,\,SF}$ and $L'_{\rm CO(2-1)}$ or $L'_{\rm CO(1-0)}$. This suggests that compact galaxies above the main sequence have enhanced star formation rates and gas masses, as expected from literature scaling relations (Magdis et al.

Table 6. Best-fitting parameters of a double-component LVG modelling of the average CO + [CI] SLEDs of $z \sim 1.25$ galaxies presented in Figs 4 and 5, and Tables 3 and 4.

Parameter	Within LTG	Within LTG, on MS	Within LTG, above MS	Compacts	Compacts, on MS	Compacts, above MS
$\log(n_{\rm H_2,low}/[{\rm cm^{-3}}])$	2.2 ± 0.2	2.2 ± 0.3	3.3 ± 0.6	3.1 ± 0.8	3.3 ± 0.8	3.0 ± 0.8
$\log(n_{\rm H_2,high}/[{\rm cm^{-3}}])$	3.9 ± 0.1	3.9 ± 0.2	4.8 ± 1.2	6 ± 1.3	5.2 ± 1.3	4.1 ± 1.6
$T_{\rm kin,\,low}/[{\rm K}]$	45 ± 98	45 ± 113	45 ± 130	180 ± 135	80 ± 135	215 ± 138
$T_{\rm kin,\,high}/[{\rm K}]$	45 ± 10	45 ± 23	250 ± 130	135 ± 138	125 ± 138	105 ± 138
$\log(M_{\rm H_2,low}/[{\rm M_\odot}])^a$	10.3 ± 0.3	10.3 ± 0.3	10.1 ± 0.2	9.7 ± 0.4	9.7 ± 0.4	9.8 ± 0.6
$\log(M_{\rm H_2,high}/[{\rm M_\odot}])^a$	10.1 ± 0.2	10.1 ± 0.3	9.6 ± 1.1	11.1 ± 1.5	10.2 ± 1.5	9.6 ± 1.8

Notes. The average values and their uncertainties are the best-fitting estimates and their statistical 1σ errors, where we impose that $n_{\rm H_2,low} < n_{\rm H_2,high}$.
[a]We note that absolute values of the gas mass from LVG modelling depend on the adopted CO abundance, constant for the various populations analysed here. Therefore, they are subject to the uncertainties already described in Section 3.4. Relative comparisons between the two phases for each population still hold, under the assumption that dense and diffuse gas reservoirs share the same metallicity.

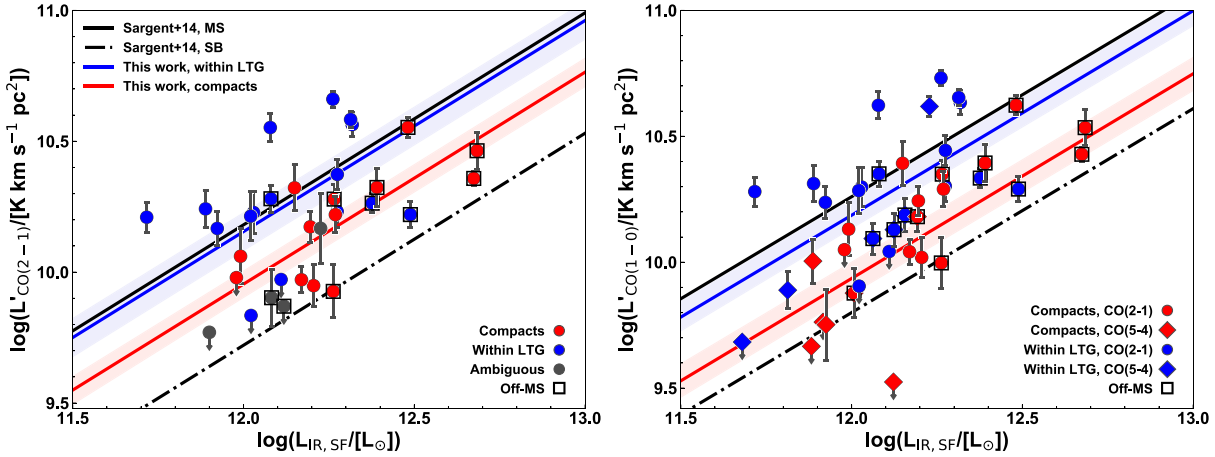

Figure 8. $L'_{\rm CO(2-1)}$ [K km s^{-1} pc^2] (left-hand panel) and $L'_{\rm CO(1-0)}$ [K km s^{-1} pc^2] (right-hand panel) luminosity as a function of the infrared luminosity from star formation $L_{\rm IR,\,SF}$ [$L_\odot$]. The solid and dashed black lines represent the models for main sequence and starburst galaxies from Sargent et al. (2014). In the left-hand panel, we convert this equation to $L'_{\rm CO(2-1)}$ using $R_{21} = 0.85$. In both panels, the blue and red solid lines are the best-fitting lines with a slope $\beta = 0.81$ obtained by fitting separately the extended and compact population, respectively. The shaded areas represent the 1σ confidence interval on the best-fitting normalization. The symbols colour-code is analogous to Fig. 3. In the right-hand panel we show with filled diamonds measurements of $L'_{\rm CO(1-0)}$ extrapolated from the CO(5-4) observed flux. The error bars in this figure correspond to the 1σ uncertainty on the CO(2-1) or CO(5-4) flux measurements.

2012; Sargent et al. 2014; Scoville et al. 2014, 2016; Genzel et al. 2015; Silverman et al. 2015b, 2018a; Tacconi et al. 2017, 2020; Elbaz et al. 2018; Franco et al. 2020; Feldmann 2020). These galaxies also lie closer to the 'strong starburst' locus, which also implies a higher star formation efficiency. On the other hand, compact galaxies within the main sequence occupy the region with low $L_{\rm IR,\,SF}$ and $L'_{\rm CO(2-1)}$ or $L'_{\rm CO(1-0)}$ along the red solid line in Fig. 8. This suggests that these sources have similar star formation efficiency (or $\tau_{\rm depl}$) to compact off-main sequence sources, but lower star formation rates and gas masses. Finally, we highlight that ambiguous objects have low CO(2-1) fluxes suggesting high star formation efficiency. Hence, these sources are likely adding to the compacts population (see also Section 3.1).

To explore the relation between the star formation efficiency, main sequence offset and compactness in our sample, we plot the $L'_{\rm CO(2-1)}/L_{\rm IR,SF}$ ratio as a function of the main sequence position and compactness in Fig. 9. As already observed in Section 3.1 for the molecular gas excitation, we find that compact galaxies within the main sequence have a $L'_{\rm CO(2-1)}/L_{\rm IR,SF}$ ratio smaller than their extended counterparts, and similar to that measured in galaxies above the main sequence. Also in this case, compact main-sequence galaxies seem to contribute to the scatter observed in the $L'_{\rm CO(2-1)}/L_{\rm IR,SF}$-$\Delta$MS relation from Valentino et al. (2020). Similar to the approach described in Section 3.1, we quantify the

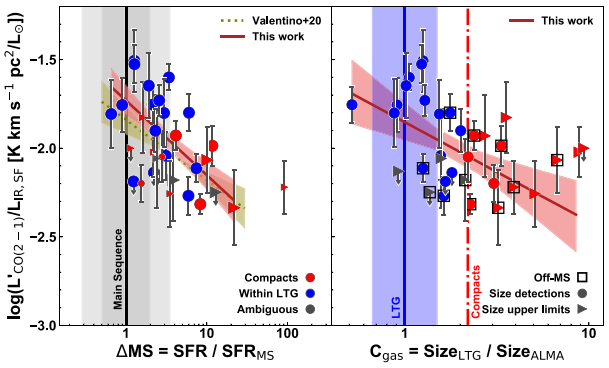

Figure 9. $L'_{\rm CO(2-1)}$ [K km s^{-1} pc^2] / $L_{\rm IR,\,SF}$ [$L_\odot$] as a function of the main sequence offset (left-hand panel) and the compactness (right-hand panel). The green dotted line and shaded area in the left-hand panel represent the best-fitting model and 1σ confidence interval from Valentino et al. (2020). The dark red solid line and shaded area in the left-hand panel indicate the $L'_{\rm CO(2-1)}$ [K km s^{-1} pc^2] / $L_{\rm IR,\,SF}$-ΔMS trend and 1σ confidence interval obtained after excluding compact and ambiguous main sequence galaxies from the fit. The dark red solid line and shaded area in the right-hand panel mark the best-fitting model and 1σ confidence interval of the $L'_{\rm CO(2-1)}$ [K km s^{-1} pc^2] / $L_{\rm IR,\,SF}$ [$L_\odot$]-$C_{\rm gas}$ trend. The colour-code and symbols are analogous to Fig. 3. We measure the uncertainty on the $L'_{\rm CO(2-1)}/L_{\rm IR,\,SF}$ ratio by propagating the 1σ errors on the CO(2-1) flux measurements and on $L_{\rm IR,\,SF}$.

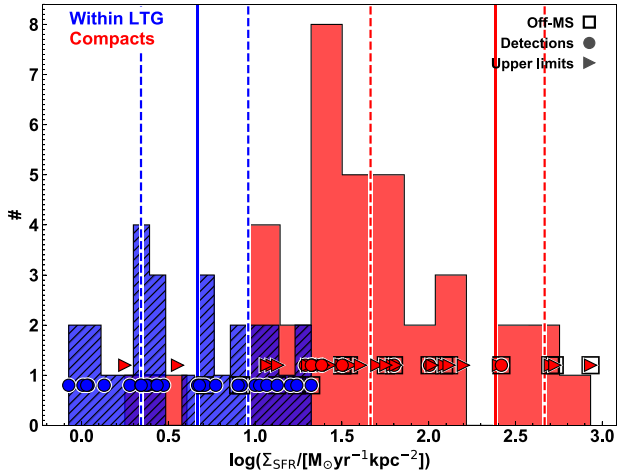

Figure 10. Star formation rate surface density distribution for compact (red) and extended (hatched blue) galaxies in our sample. The solid and dashed lines indicate the median and interquartile range of each distribution, respectively. Measurements and upper limits are highlighted with circles and triangles, respectively. The open black squares indicate galaxies above the main sequence, with ΔMS$\geq$3.5.

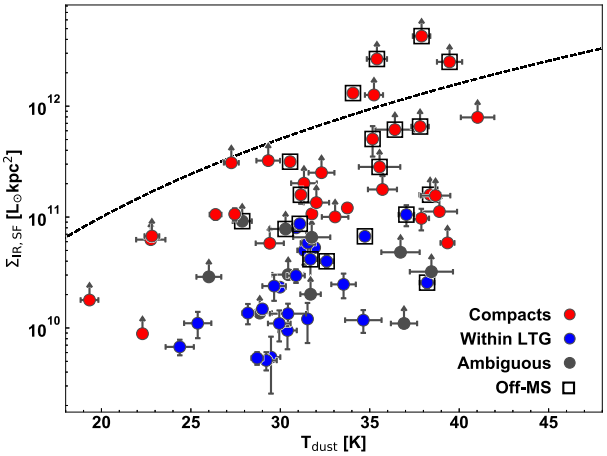

Figure 11. IR luminosity surface density as a function of the dust temperature for our sample. The colour-code is analogous to Fig. 3. The dashed line represents the Stefan-Boltzman law for optically thick dust clouds.

contribution of compact main-sequence galaxies to the scatter of the $L'_{CO(2-1)}/L_{IR,SF}$-ΔMS trend by fitting the $L'_{CO(2-1)}/L_{IR,SF}$ ratio as a function of the main sequence offset excluding the compact and ambiguous galaxies within the main sequence scatter and the strongest outlier. As for the previous case, excluding these sources from the fit improves the correlation between $L'_{CO(2-1)}/L_{IR,SF}$ and ΔMS (see Table 2). We also find a slightly steeper slope and smaller intrinsic scatter than the trend reported in Valentino et al. (2020). The right-hand panel of Fig. 9 shows that the $L'_{CO(2-1)}/L_{IR,SF}$ ratio decreases as a function of the compactness (red line in Fig. 9, see also Table 2). We note that the slope of this correlation ($\beta = -0.56$) seems steeper than the slope of the $L'_{CO(2-1)}/L_{IR,SF}$ versus ΔMS correlation ($\beta = -0.42$, red line in the left-hand panel of Fig. 9). This is only a suggestion at this stage, however, due to the large uncertainties associated with this parameter.

3.3 Star formation rate surface density, intensity of the radiation field, and dust temperature

We measure the star formation rate surface density by dividing the far-infrared star formation rate by the area $\Sigma_{SFR} = SFR/(2\pi R^2_{eff})$, where R_{eff} is the ALMA effective radius. In Fig. 10 we show the star formation rate surface density distribution for our sample. The median star formation rate surface density is $\Sigma_{SFR} = 242^{+223}_{-196}$ $M_\odot yr^{-1}kpc^{-2}$ for compact galaxies and $\Sigma_{SFR} = 5^{+5}_{-3}$ $M_\odot yr^{-1}kpc^{-2}$ for the extended population, with error bars indicating the interquartile range of the distribution. A log-rank test to the two distributions, accounting for the presence of upper limits on Σ_{SFR} shows that the two distributions are significantly different (p-value < 0.001). This shows that compact galaxies have enhanced star formation rate surface density with respect to extended galaxies and similar to local (U)LIRGs (e.g. Liu, Gao & Greve 2015a) and galaxies above the main sequence at high redshift (Jiménez-Andrade et al. 2019). This is somewhat expected, since compact and extended galaxies have similar star formation rates (Fig. 2) while very different submillimetre sizes (Fig. 1). This fits the idea that the compactness allows us to identify starburst galaxies, as discussed in Section 4.

In Fig. 11, we show the far-infrared surface density as a function of the dust temperature. Here, T_{dust} is derived from the intensity of the radiation field $\langle U \rangle = (T_{dust}/18.9\,K)^{6.04}$, following Magdis et al. (2017). Fig. 11 shows that compact galaxies have higher infrared surface density than extended galaxies. The infrared surface density of compact galaxies is instead similar to that measured in starbursts and submillimetre galaxies at high redshift (Ikarashi et al. 2015; Simpson et al. 2017; Hodge et al. 2019; Jin et al. 2019). We note that some compact galaxies in Fig. 11 lie above the limit for optically thick dust clouds. This might suggest that these galaxies are optically thick and their dust temperature is even warmer than what inferred from the peak of the far-infrared SED. As a result, the dust mass in those object might be overestimated (Jin et al. 2019; Cortzen et al. 2020). The overall distribution of compact galaxies is somewhat skewed towards high values of dust temperatures. For the compact galaxies we find a median $T_{dust} = 34 \pm 4$ K, while for the extended population $T_{dust} = 31 \pm 1$ K with the uncertainties corresponding to the interquartile range of the dust temperature distributions of each population.

Fig. 12 shows that compact galaxies have higher intensity of the radiation field than extended galaxies. For the compact galaxies we find a median $\langle U \rangle = 33^{+33}_{-19}$, while for the extended population $\langle U \rangle = 19^{+4}_{-5}$. The uncertainties indicate the interquartile range of the distributions. The intensity of the radiation field is a metallicity-weighted measurement of the star formation efficiency (Magdis et al. 2012). Therefore, Fig. 12 provides additional indications of the fact that compact galaxies have enhanced star formation efficiency with respect to the extended population.

3.4 Gas content

The mass of the molecular gas reservoir is a crucial quantity to understand the future evolution of galaxies. However, measuring the amount of molecular gas in galaxies is notoriously a difficult task (see e.g. Birkin et al. 2021). This stems from the fact that measuring the molecular gas mass requires choosing an observable-to-gas conversion factor depending on the molecular gas tracer adopted. When inferring gas masses from the CO luminosity or the dust mass, for example, one needs to assume a CO-to-H_2 or a gas-to-dust ratio (α_{CO} and δ_{GDR}, respectively). Both conversion factors have complex dependencies on e.g. the state of the ISM, the gas-phase metallicity,

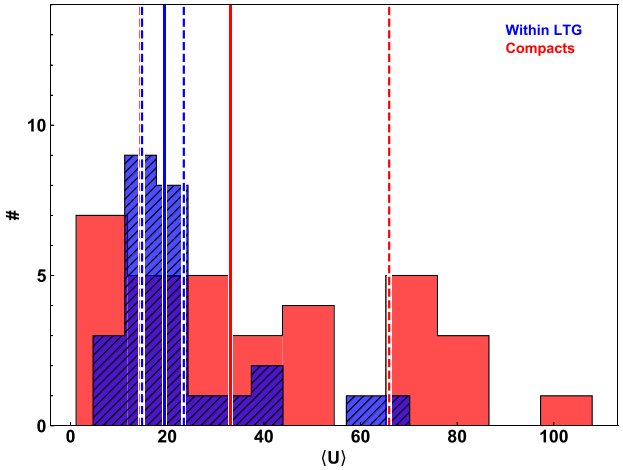

Figure 12. Distribution of the intensity of the radiation field for compact (red) and extended (hatched blue) galaxies in our sample. The solid lines indicate the median of each distribution. The dashed lines represent the interquartile ranges.

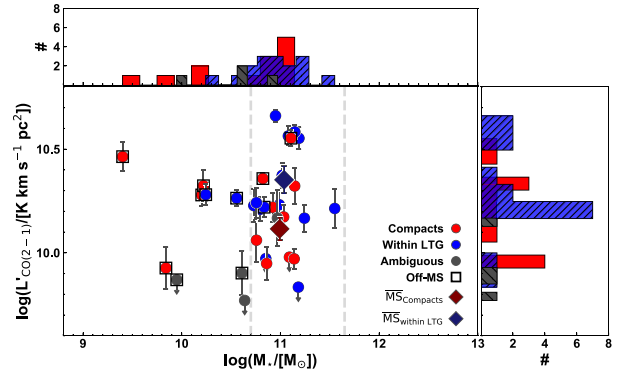

Figure 13. $L'_{CO(2-1)}$ [K km s^{-1} pc^2] as a function of the stellar mass. Large filled diamonds are the average $L'_{CO(2-1)}$ luminosities for compact and extended main sequence galaxies with $M_\star \geq 5 \times 10^{10}\,M_\odot$. Vertical dashed grey lines highlight the $M_\star$ range considered for computing average $L'_{CO(2-1)}$ values. The blue circles highlight extended galaxies. The red circles indicate the compacts. The grey large circles represent ambiguous sources. The open black squares highlight galaxies with ΔMS$\geq$3.5. The error bars represent the 1σ uncertainty on the CO(2-1) flux. The upper histogram indicate the $M_\star$ distribution of galaxies in our sample, split according to their compactness. The histogram on the right indicate their $L'_{CO(2-1)}$ distribution.

or galaxy type (Leroy et al. 2011; Magdis et al. 2012; Narayanan et al. 2012; Bolatto, Wolfire & Leroy 2013; Genzel et al. 2015; Silverman et al. 2018b) that are not yet fully understood. For this reason, we first explore the molecular gas properties of our sample by considering observed $L'_{CO(2-1)}$ luminosities as a proxy. We also use M_{dust} as an independent tracer of the molecular gas reservoir.

3.4.1 *Observed quantities*

The analysis performed in the previous sections suggests that compacts are characterized by a highly excited ISM, enhanced star formation efficiency and shorter depletion time. Also, compact galaxies within the main sequence seem underluminous in CO(2-1), possibly suggesting that their gas content is reduced. However, the gas fraction is predicted to decrease with stellar mass (e.g. Magdis et al. 2012; Tacconi et al. 2017; Liu et al. 2019, Tacconi et al. 2020, and references therein). To understand whether the trends observed in the previous sections are driven by the stellar mass, we plot in Fig. 13 the $L'_{CO(2-1)}$ luminosity as a function of the stellar mass for our sample. Despite the scatter, this plot confirms that compact main sequence galaxies are less luminous in $L'_{CO(2-1)}$ than extended and compact off-main sequence galaxies with similar stellar mass, on average. To quantify this effect, we compute the average $L'_{CO(2-1)}$ luminosity of compact and extended galaxies within the main sequence. For this computation, we consider only galaxies with $M_\star \geq 5 \times 10^{10}\,M_\odot$ to account for the fact that the gas fraction (hence $L'_{CO(2-1)}$) decreases as a function of the stellar mass. This results in 7 compact and 13 extended galaxies within the main sequence with an average stellar mass of $M_\star = 10^{11}\,M_\odot$. We find $L'_{CO(2-1),compacts,MS} = 1.3 \pm 0.2 \times 10^{10}$ [K km s^{-1} pc^2] and $L'_{CO(2-1),extended,MS} = 2.2 \pm 0.3 \times 10^{10}$ [K km s^{-1} pc^2].[3] That is, compact main sequence galaxies are $\sim$1.7 $\times$ less luminous in CO(2-1) at $\sim 5\sigma$ significance.

Finally, in Fig. 14 we show the ratio between the $L'_{CO(2-1)}$ luminosity and stellar mass as a function of the main sequence offset and the compactness. In addition, we show the ratio between the dust and stellar mass as a function of the same quantities. The top left-hand panel of Fig. 14 shows that the $L'_{CO(2-1)}/M_\star$ ratio increases as a function of the main sequence offset. Compact galaxies on the main sequence, on the other hand, seem to be underluminous in CO(2-1) with respect to extended sources. We find a similar trend for the $M_{dust}/M_\star$ ratio in the bottom left-hand panel of Fig. 14. In the right-hand panels of this figure we see that both the $L'_{CO(2-1)}/M_\star$ and $M_{dust}/M_\star$ ratios decrease as a function of the compactness, albeit with a large scatter.

3.4.2 *Derived quantities*

Building on the results presented in the previous sections, we now convert CO luminosities and dust masses into gas masses by adopting conversion factors that are appropriate for the excitation conditions and star formation efficiency properties of each galaxy. Clearly our approach will still suffer from the classical uncertainties related to the choice of the observable-to-gas conversion factors. However, the detailed knowledge of the molecular gas properties of both individual galaxies in our sample (see Table 1) and the availability of average CO SLEDs for each of the galaxy sub-populations analysed in this work allow us to physically motivate the choice of α_{CO}/δ_{GDR} for each galaxy class. A detailed analysis of the α_{CO}/δ_{GDR} conversion factors in individual sources will be presented in future papers. We highlight here that a common approach in literature is to use the main sequence position of a source to define the preferred observable-to-gas conversion factor (e.g. Magnelli et al. 2012; Sargent et al. 2014; Accurso et al. 2017; Aravena et al. 2019; Cassata et al. 2020). While this might appear a reasonable assumption lacking additional constraints on the galaxy ISM conditions, we urge caution against this approach considering that galaxies within the main sequence display a wide range of compactnesses, CO excitations, and star formation efficiencies.

When inferring CO-based gas masses, we only consider galaxies with CO(2-1) observations because this low-J transition is directly tracing the total molecular gas reservoir. We convert $L'_{CO(2-1)}$ to $L'_{CO(1-0)}$ using $R_{21} = L'_{CO(2-1)}/L'_{CO(1-0)} = 0.85$. We then compute

[3]Formally biased estimators as we turned the first upper limit into a detection to compute the mean value of the distribution.

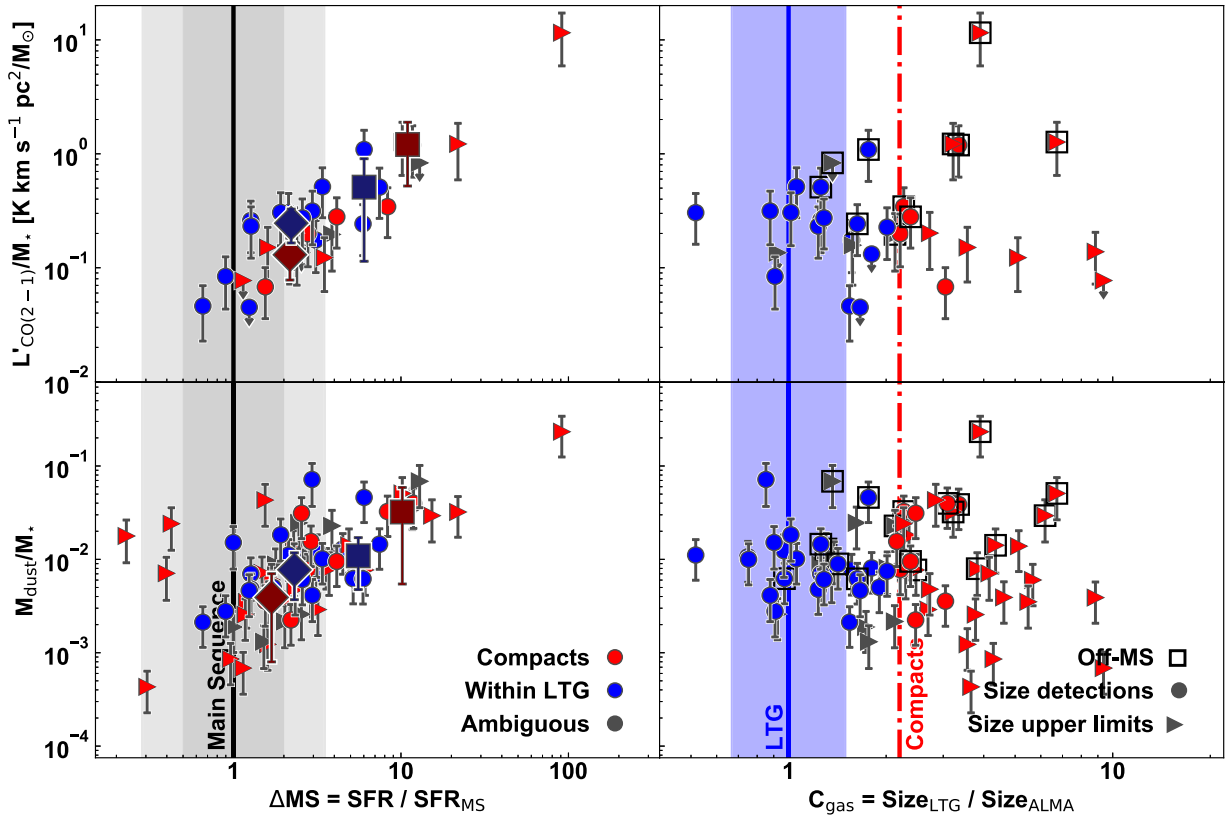

Figure 14. Top row: $L'_{CO(2-1)}/M_\star$ ratio as a function of the main sequence offset (left-hand panel) and the compactness (right-hand panel). Bottom row: $M_{dust}/M_\star$ ratio as a function of the main sequence offset (left-hand panels) and the compactness (right-hand panels). In the left-hand panels, large filled diamonds indicate median $L'_{CO(2-1)}/M_\star$ and $M_{dust}/M_\star$ ratios for extended and compact galaxies with $1 \leq \Delta MS \leq 3.5$ while large filled squares indicate median gas fractions for extended and compact sources with $\Delta MS \geq 3.5$ (dark blue and dark red symbols, respectively). The colour code and symbols for individual data points are analogous to Fig. 3. The error bars associated to the individual data points are obtained by propagating the 1σ uncertainty on the CO(2-1) flux measurements and a 0.2 dex uncertainty on the stellar mass.

the gas mass as $M_{gas} = \alpha_{CO} \times L'_{CO(1-0)}$. We adopt $\alpha_{CO} = 3.6\ M_\odot$(K km s^{-1}pc^2)$^{-1}$ for extended galaxies since this value has been suggested to be appropriate for high-redshift, highly star-forming discs (e.g. Daddi et al. 2015). Ambiguous and compact galaxies are instead characterized by a compact CO emission, enhanced CO excitation, and high $L'_{CO(2-1)}/L_{IR,SF}$ ratios, resembling the ISM conditions of starbursting objects in the local Universe for which $\alpha_{CO} = 0.8\ M_\odot$(K km s^{-1}pc^2)$^{-1}$ (Solomon et al. 1987). Indeed, a starburst-like α_{CO} has been shown to be appropriate for compact galaxies at high redshift (Tadaki et al. 2017b).

When computing gas masses from the dust mass, we consider only galaxies with a reliable dust mass measurement ($M_{dust}/M_{dust,\,err} \geq 5$). This corresponds to 69 galaxies, significantly improving the statistics with respect to CO-based gas mass estimates. We compute the gas mass as $M_{gas} = \delta_{GDR} \times M_{dust}$, following Magdis et al. (2012). We adopt $\delta_{GDR} = 85$ for the extended population, corresponding to a metallicity-dependent gas-to-dust ratio at $Z = 12 + \log(O/H) = Z_\odot$ (Magdis et al. 2012). On the other hand, we use $\delta_{GDR} = 30$ for compact and ambiguous galaxies since we show that these have 'starburst-like' ISM conditions such as an enhanced CO excitation (as seen from both individual R_{52} ratios and average CO SLEDs, see Section 3.1), enhanced efficiency (see Section 3.2), high SFR, and infrared surface density, dust temperatures, and intensity of the radiation field (see Section 3.3), and starbursts at high redshift are reported to have supersolar metallicities (Puglisi et al. 2017).

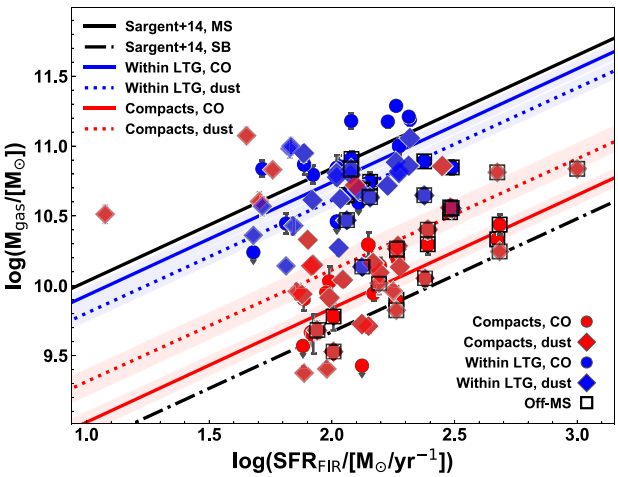

Figure 15. Inverse, integrated Schmidt–Kennicutt relation between the star formation rate and the molecular gas mass. The coloured filled circles show gas masses derived from CO lines. The coloured filled diamonds indicate dust-based gas masses. We report both CO-based and dust-based gas masses when available. The blue and red solid (dotted) lines represent the best-fitting lines with a slope $\beta = 0.81$ obtained by fitting the CO- (dust-) based gas mass measurements for the extended and compact population, respectively. The shaded areas represent the 1σ confidence interval on the best-fitting normalizations.

In Fig. 15, we show the correlation between the molecular gas mass and the star formation rate for our sample, that, is the integrated Schmidt–Kennicutt relation considering derived quantities rather than pure observables (as instead shown in Fig. 8). Here we measure gas masses from both CO lines and dust masses, when available. The inclusion of dust-based molecular gas masses allows us to study the relation between the gas mass and SFR with increased statistics with respect to gas mass measurements from the CO(2-1). We note that Fig. 15 would be equivalent to show the 'resolved' Schmidt–Kennicutt relation considering the molecular gas and star formation rate surface densities for our sample. This is because we find that molecular gas sizes (as sampled by the dust continuum) and SFR sizes (traced by the CO(5-4) emission) are nearly equivalent for our galaxies (see Section 2.1.1), and therefore both axes would be rescaled by the same quantity. This plot confirms the results of Fig. 8 that extended and compact galaxies have different star formation efficiency properties. These galaxies occupy distinct regions of the integrated Schmidt–Kennicutt plane and the offset increases when translating observables into physical quantities, accounting for the ISM properties of each source. In particular, if we consider CO-based molecular gas masses, we obtain that the normalization of the $\log(M_{\rm gas})$-β $\times$ $\log(\rm SFR_{FIR})$ relation is 8.21 ± 0.08 for compact galaxies and 9.12 ± 0.07 for extended sources (red and blue solid lines in Fig. 15, respectively). The average offset of compact galaxies with respect to the locus for extended sources is 0.91 dex. This corresponds roughly to a factor of 8 enhancement in star formation efficiency, further stressing the starbursting nature of the ISM in these sources. When considering dust-based molecular gas masses, the offset of compact galaxies reduces to 0.5 dex or a factor of 3.2 star formation efficiency enhancement, on average (see red and blue dotted lines in Fig. 15). However, the fit seems to be driven by a small number of compact galaxies with a high gas mass in this case. These sources might have been misclassified as compacts since they lie only $\sim 1\sigma$ below the mass–size relation (see also Fig. 16). Alternatively, this might reflect the fact that the separation between compact and extended galaxies is not purely bimodal. However, we still observe that most compact galaxies are shifted towards the starburst locus in the Sargent et al. (2014) model.

We define the gas fraction as $\mu_{\rm gas} = \frac{M_{\rm gas}}{M_\star}$ and we show this quantity as a function of the main sequence offset and the compactness in Fig. 16. To quantify the difference in the gas fraction of compact and extended galaxies on and above the main sequence, we split our sample in two ΔMS bins and we compute the average gas fraction of compact and extended sources within each bin. When considering CO-based gas fractions, we find $\mu_{\rm gas,\,Compacts,\,MS} = 0.12 \pm 0.05$ and $\mu_{\rm gas,\,Extended,\,MS} = 1.04 \pm 0.34$ for compact and extended galaxies within the main sequence. If we consider dust-based gas masses, we find $\mu_{\rm gas,\,Compacts,\,MS} = 0.12 \pm 0.09$ and $\mu_{\rm gas,\,Extended,\,MS} = 0.66 \pm 0.34$. That is, compact galaxies have $\sim 6-9\times$ reduced gas fractions with respect to extended sources, in agreement with previous results for small samples of one or two compact galaxies (Popping et al. 2017; Tadaki et al. 2017b; Brusa et al. 2018, for CO-based gas fractions). The median gas fractions are different at $1.2-2.7\sigma$ significance. On the other hand, galaxies above the main sequence (ΔMS$\geq$3.5) have similar gas fractions as we obtain $\mu_{\rm gas,\,Compacts,\,off\text{-}MS} = 1.14 \pm 0.70$ and $\mu_{\rm gas,\,Extended,\,off\text{-}MS} = 2.2 \pm 1.7$ when considering the CO(2-1) luminosity as a molecular gas tracer. This is confirmed when considering dust masses as proxies for the molecular gas ($\mu_{\rm gas,\,Compacts,\,off\text{-}MS} = 0.97 \pm 0.80$ and $\mu_{\rm gas,\,Extended,\,off\text{-}MS} = 0.93 \pm 0.52$). We also find a tentative trend of decreasing gas fraction as a function of the compactness when considering both CO(2-1) luminosities and dust masses. We explore the dependence of $\mu_{\rm gas}$ on the compactness by applying a linear regression analysis to the bottom panel of Fig. 16, owing to the larger statistics available when considering the dust mass as a gas mass tracer. Indeed, we find a correlation between the gas fraction and the compactness. The results are reported in Table 2 and the best-fitting correlation is shown as a red solid line in the right-hand panel of Fig. 16.

A small number of compact galaxies within the main sequence show 'main sequence like' gas fractions when considering dust-based measurements. These sources lie only 1σ below the mass–size relation and are close to the compactness limit that we use to discriminate between compact and extended galaxies (red dash-dotted line in the right-hand panels of Fig. 16, e.g.). Hence, these could have been misclassified (due to e.g. noise in the ALMA size measurements) and might rather belong to the extended sample. Alternatively our data might suggest that galaxies do not follow a bimodal distribution, but are gradually distributed in the $\mu_{\rm gas}$–$C_{\rm gas}$ plane similar to our previous findings (see Fig. 15 and e.g. fig. 3 in Valentino et al. 2020). This seems to be suggested by the right-hand panel of Fig. 16 where we see that $\mu_{\rm gas}$ broadly decreases as a function of the compactness. However, we argue that Fig. 16 overall suggests a more complex dependence of the gas fraction on galaxy properties, possibly as a result of evolutionary trends. We will explore this aspect in Section 4.

We finally note that the difference in $\mu_{\rm gas}$ between compact and extended galaxies on the main sequence depends on the choice of the $\delta_{\rm GDR}$ or $\alpha_{\rm CO}$ conversion factors. In particular, the tension between compact and extended galaxies within the main sequence is reduced to a factor of 2 when considering metallicity-dependent conversion factors (see Appendix A). However, the extensive analysis of the ISM conditions presented in the previous sections, the results obtained from the observables as well as the agreement between molecular gas tracers when using observables-to-gas conversion factors tailored to the compactness properties of each source (see Figs A2 and A3) corroborate our choice of the conversion factors for each galaxy subsample. Finally, the use of different conversion factors for compacts and extended galaxies is also corroborated by the results presented in Fig. 8 and 15, suggesting that these sources have different star formation efficiency properties.

4 DISCUSSION

4.1 The role of compactness in galaxy evolution

While the ISM properties of galaxies at $z \sim 1.3$ are weakly correlated with the offset from the main sequence (Valentino et al. 2020), a diversity of ISM properties has been observed within the main sequence scatter itself (Elbaz et al. 2018; Puglisi et al. 2019). In agreement with these results, here we find that ~ 46 per cent[4] of galaxies in our sample have a compact molecular gas reservoir. These galaxies have excited CO line ratios, enhanced star formation efficiencies, and are spread on and above the main sequence blurring the R_{52} and $L'_{\rm CO(2-1)}/L_{\rm IR,SF}$ versus ΔMS correlations (see Figs 3 and 9). These results suggest that galaxies within the main sequence scatter are not all largely unperturbed gas-rich discs. However, this does not seem to be simply due to a large scatter in the properties of star-forming galaxies. Our results suggest instead that the diversity

[4]This number would actually be even larger if one would consider galaxies with loose size upper limits as submillimetre compact sources, see also Section 3.1.

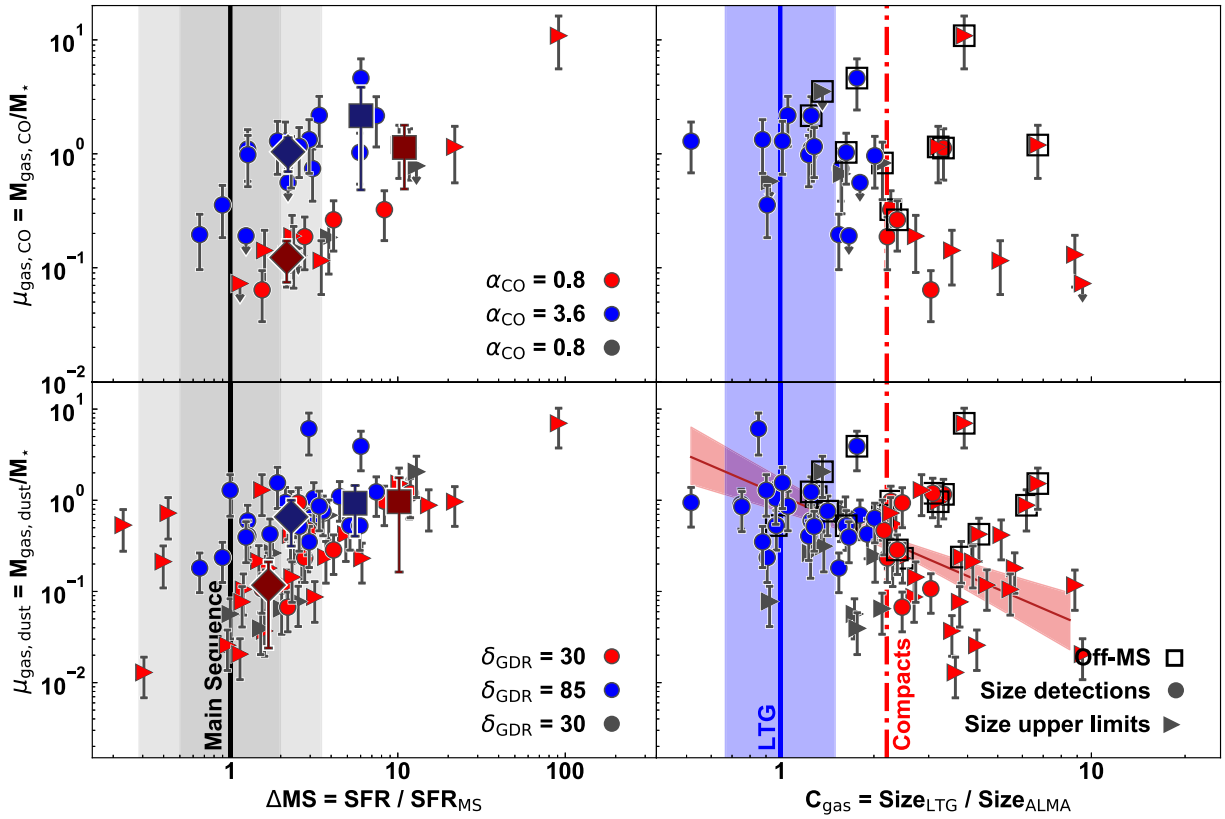

Figure 16. Gas fractions from $L'_{CO(2-1)}$ [K km s^{-1} pc^2] (top row) and M_{dust} [M$_\odot$] (bottom row), as a function of the main sequence offset (left-hand panel) and the compactness (right-hand panel). We convert $L'_{CO(2-1)}$ or M_{dust} to a gas mass by assuming α_{CO} or δ_{GDR} conversion factors tailored to the compactness properties of each source, as reported in the legend. Symbols and colour-code are analogous to Fig. 14. Similar to Fig. 14, error bars in this plot are obtained by propagating the 1σ error on the CO flux and a typical 0.2 dex uncertainty on the stellar mass. Therefore, the error bars do not account for the systematic uncertainty associated to the α_{CO} or δ_{GDR} conversion factors.

of gas excitation conditions and efficiency observed in MS galaxies is associated with the compactness of the molecular gas reservoir. Indeed, excluding submillimetre compact galaxies from the fits in Figs 3 and 9 improves the correlation between galaxy ISM properties and the main sequence offset. Furthermore, we find correlations between galaxy ISM properties and the submillimetre compactness (see Table 2). Distinguishing galaxies for their submillimetre compactness also allows us to select objects with significantly different CO SLEDs (see Figs 4 and 5). These results suggest that the compactness of the molecular gas reservoir traces the ISM state of a source. We thus suggest here that using a submillimetre compactness threshold:

$$C_{gas} = \frac{R_{eff,vdW+14}(z)}{R_{eff,ALMA}} = \frac{A(z) \times (M_\star/7 \times 10^{10} M_\odot)^{\alpha(z)}}{R_{eff,ALMA}} \geqslant 2.2 \quad (2)$$

would allow us to better distinguish between high redshift, gas-rich discs and galaxies harbouring a highly excited, starbursting ISM. Here $A(z)$ and $\alpha(z)$ are the best-fitting coefficients for the mass–size relation of van der Wel et al. (2014). The value $C_{gas} = 2.2$ corresponds to $\sim$1σ below the optical mass–size relation of discs. We note that this proposed criterion is qualitatively similar to using the star formation rate surface density (Σ_{SFR}) to select starbursting sources (e.g. Jiménez-Andrade et al. 2019; Valentino et al. 2020, and references therein). In fact, compact galaxies have higher star formation rate surface density than extended sources (see e.g. Fig. 10). However, considering the submillimetre compactness as in equation (2) allows us to account for the stellar mass dependence of the star formation rate and size thus rescaling to the structural properties of each object.

In line with our results, various studies (e.g. Downes & Solomon 1998; Combes et al. 2013; Narayanan & Krumholz 2014; Bournaud et al. 2015) have highlighted the importance of the star formation rate surface density as a proxy for the star formation properties of galaxies since this parameter depends on the gas density, temperature, and optical depth (Narayanan & Krumholz 2014).

One caveat here is that, as a result of the far-infrared selection, our observations sample the upper stripe of the main sequence scatter at $M_\star \sim 5 \times 10^{10} M_\odot$. Our observations fully probe the 1σ scatter of the main sequence ($\pm$0.3 dex) only at $M_\star \geq 10^{11} M_\odot$. Similar to previous ALMA studies at high redshift (e.g. Elbaz et al. 2018; Tadaki et al. 2020), our sample thus appears to be biased towards highly star-forming massive galaxies and it might be not trivial to extrapolate our results to lower stellar mass regimes. This is because the high-mass end of the main sequence is the locus where galaxies are expected to quench soon (Dekel & Birnboim 2006; Zolotov et al. 2015), and/or where the more numerous population of passive galaxies might be temporarily boosted by rejuvenation (Mancini et al. 2019). Deeper observations of mass-selected samples at $M_\star \leq 10^{10} M_\odot$ will be required to understand if our results apply to the main sequence population at lower stellar mass.

4.2 On the nature of submillimetre compact galaxies within the MS

As discussed in the introduction, the discovery of a significant number of submillimetre compact galaxies within the scatter of

the main sequence conflicts with the idea that galaxies along this sequence are mostly secularly evolving discs. The lack of a clear trend between galaxy ISM properties and the main sequence offset seems to disfavour alternative scenarios according which galaxies oscillate around the main sequence as a result of compaction episodes (e.g. Tacchella et al. 2016). It has also been proposed that submillimetre compact main sequence galaxies are the result of major mergers with a moderate star formation rate enhancement because of the enhanced gas fractions (Jiménez-Andrade et al. 2019). While some of the submillimetre compact main sequence galaxies in our analysis might be consistent with being 'failed burst' mergers, this would fail to explain why most of these sources have a reduced gas fraction (see Fig. 16).

The investigation of the ISM conditions presented in this paper allows us to shed light on possible formation mechanisms of such objects. Submillimetre compact galaxies on and above the main sequence have remarkably similar excitation properties (see in particular Fig. 5 and Table 5) and star formation efficiency (see Section 3.2) and these properties are enhanced with respect to those of extended galaxies. This hints at a common origin between submillimetre compact galaxies on and above the main sequence, likely associated to a merger event. Mergers are in fact capable of inducing strong inflows to the nuclear regions reducing significantly the size of the molecular gas reservoir and enhancing the efficiency of star formation (Mihos & Hernquist 1996). Merger-driven starbursts are also predicted to have larger gas excitations than highly star-forming discs due to the prevalence of compressive tides enhancing the density of the gas (Bournaud et al. 2015). On the other hand, submillimetre compact galaxies within the main sequence with $M_\star \geq 10^{10.7} M_\odot$ are underluminous in $L'_{\rm CO(2-1)}$ for their stellar mass and SFR (see Figs 13 and 14) translating into reduced gas fractions (see Fig. 16). The reduced gas fractions of submillimetre compact galaxies within the main sequence would naturally result from efficient gas consumption during the preceding starburst phase. Furthermore, when fitting a linear function in the $\log(\mu_{\rm gas})$–$\log(\Delta{\rm MS})$ plane, we find that submillimetre compact galaxies have a larger intrinsic scatter than extended sources ($\sigma_{\rm int,\,Compacts} = 0.49 \pm 0.08$ versus $\sigma_{\rm int,\,Extended} = 0.22 \pm 0.09$ in Fig. 16). This fits the idea that submillimetre compacts within the main sequence are the relic of a previous starburst episode, as in this case we expect to detect sources in different stages of the post-starburst phase.

Therefore, the results of this paper support the scenario proposed in Puglisi et al. (2019) and suggest that submillimetre compact massive galaxies within the main sequence represent transient objects in an 'early post-starburst phase' following a merger-driven starburst episode (see also Elbaz et al. 2018 and Franco et al. 2020). We schematically summarize this proposed evolutionary trend in Fig. 17. Our results and proposed scenario are consistent with cosmological simulations suggesting that compact galaxies form by repeated major mergers of small progenitors (Chabanier et al. 2020). These simulations predict gas fractions of ~ 20 per cent in compact star-forming galaxies versus ~ 50 per cent for extended main-sequence galaxies at $z \sim 2$, as a result of gas consumption by star formation, as well as gas exhaustion in major mergers which can efficiently consume and/or expel gas and in good agreement with our results.

A visual inspection of the *HST* imaging available for this sample does not reveal any clear evidence of an enhanced merger fraction in the submillimetre compact population within the main sequence. However, this does not necessarily contradict the idea that submillimetre compact galaxies are associated to mergers. In fact, only F814W *HST* imaging is homogeneously available for the full sample, sampling the rest-frame UV emission at $z \sim 1.3$. Therefore, strong

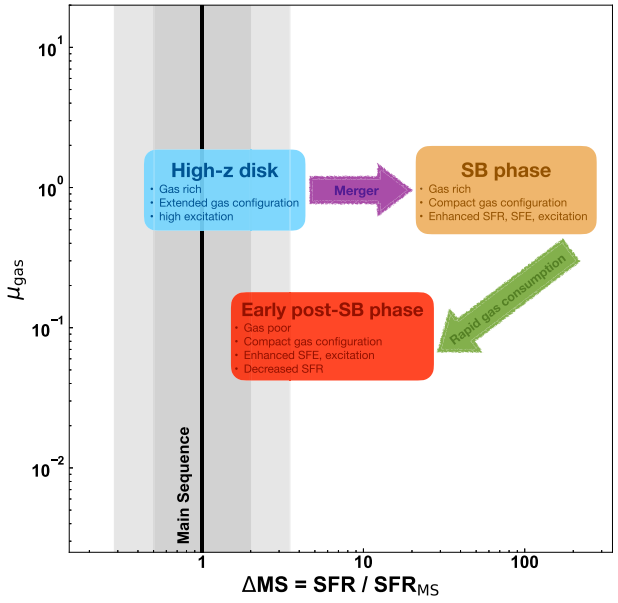

Figure 17. A schematic figure summarizing how the gas fraction evolves as a function of the main sequence offset according to our proposed evolutionary scheme. Strong gravitational perturbations (i.e. a major merger) induce an enhancement of the ISM excitation, star formation efficiency, and of the star formation rate, and push the galaxy above the main sequence. The galaxy is gas-rich, has a compact molecular gas reservoir, and moves roughly horizontally across the plane. The galaxy rapidly consumes the gas and reduces its star formation rate while retaining a compact molecular gas configuration, enhanced star formation efficiency, and ISM conditions. The galaxy goes back to the main sequence, moving to the bottom left-hand corner of the plane.

dust attenuation effects might hamper an accurate merger classification (e.g. Cibinel et al. 2019). Furthermore, in our proposed interpretation, submillimetre compact galaxies within the main sequence are 'early post-starburst' galaxies, hence likely observed at or somewhat past the coalescence phase. Therefore, we would not necessarily classify these sources as mergers. In fact, morphological classification criteria are able to identify mergers up to the coalescence phase, hence before disturbances or asymmetries in the imaging fade away (see discussion in Puglisi et al. 2019, and references therein). On the other hand, the $L'_{\rm CO(5-4)}/L_{\rm IR,SF}$ ratio might provide further indications on the evolutionary stage of our sources. Fig. 18 shows the distribution of the $L'_{\rm CO(5-4)}/L_{\rm IR,SF}$ logarithmic ratio for galaxies in our sample, distinguished for their submillimetre compactness. We measure $\log(L'_{\rm CO(5-4)}/L_{\rm IR,SF}/[{\rm K\,kms^{-1}pc^2}]/{\rm L_\odot}) = -2.6^{+0.4}_{-0.1}$ in submillimetre compact galaxies and $\log(L'_{\rm CO(5-4)}/L_{\rm IR,SF}/[{\rm K\,kms^{-1}pc^2}]/{\rm L_\odot} = -2.5^{+0.10}_{-0.2})$ in submillimetre extended sources. Furthermore, we apply a log-rank test to the two distributions, accounting for the presence of upper limits on the $\log(L'_{\rm CO(5-4)}/L_{\rm IR,SF})$ ratio and we find a ~ 87 per cent probability that the two distributions are different (p-value = 0.13). That is, we find marginal evidence that submillimetre compact galaxies have lower $L'_{\rm CO(5-4)}/L_{\rm IR,SF}$ ratio compared to submillimetre extended sources. The CO(5-4) luminosity correlates linearly with the far-infrared luminosity from star formation and this has been interpreted as an evidence that $L'_{\rm CO(5-4)}$ traces dense, star-forming molecular gas (Bayet et al. 2009; Greve et al. 2014; Daddi et al. 2015; Liu et al. 2015b; Cassata et al. 2020; Valentino et al. 2020). Therefore, this might suggest that the submillimetre compact population is caught in a declining phase of the starburst since the 'instantaneous star formation rate', as traced by the CO(5-4) luminosity (Daddi et al.

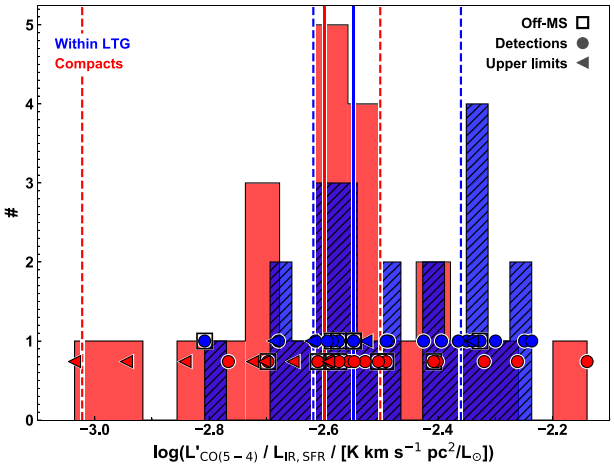

Figure 18. Distribution of the $L'_{CO(5-4)}/L_{IR,SF}$ logarithmic ratio for submillimetre compact (red) and extended (hatched blue) galaxies in our sample. The solid and dashed lines indicate the median and interquartile range of each distribution, respectively. The $\log(L'_{CO(5-4)}/L_{IR,SF})$ measurements and upper limits are highlighted with circles and triangles, respectively. The open black squares indicate galaxies above the main sequence, with $\Delta MS \geq 3.5$.

2015), is lower than the star formation rate averaged on a ∼100 Myr time-scale, as traced by the far-infrared luminosity (Kennicutt 1998). However, we measure a difference only at the $\sim 2\sigma$ level. Future studies with larger statistics will allow us to confirm this result.

We note that compact star-forming galaxies at high redshift have already been proposed as a key population for our understanding of massive, quenched galaxies formation (Barro et al. 2013, 2014, 2016; Nelson et al. 2014; van Dokkum et al. 2015). These so-called 'blue nuggets' are however selected for their compact size in the optical. This selection might be therefore biased to a later phase of the quenching process where the compact stellar core has been already formed. Conversely, our selection seems to identify an early phase of the compact core build-up (see Fig. 1). This might explain why extended SFGs and 'blue nuggets' present similar ISM conditions except than in the radio regime which samples the starburst activity on longer time-scales (0–400 Myr, see Gómez-Guijarro et al. 2019, and references therein). The radio properties of 'blue nuggets' suggest that these galaxies are old starbursts (Gómez-Guijarro et al. 2019) and might indicate the existence of an evolutionary link between submillimetre compacts, optically compact galaxies, and passive ellipticals.

Selecting compact galaxies by means of the molecular gas size likely allows us to identify galaxies in an early phase of the transition to a passive, bulge dominated galaxy retaining the imprints of their formation mechanism. Future studies of this population will provide a new perspective for our understanding of quenching processes and passive galaxies formation which typically display post-starburst features (Belli, Newman & Ellis 2019; D'Eugenio et al. 2020). A possible connection with the quenched population is also suggested by the tentative evidence that submillimetre compact galaxies have an enhanced AGN fraction (see Fig. 1), in agreement with recent literature results (Elbaz et al. 2018; Scholtz et al. 2020). Consistently with this result, major mergers can in fact enhance the accretion activity on to the central black hole (Springel & Hernquist 2005) and expel large quantities of gas via, e.g. tidal tails (Puglisi et al. 2021) affecting the future star formation processes in the remnant. Finally, the existence of an evolutionary link between 'submillimetre compact' and quenched galaxies might also be suggested by the extremely compact size of high-redshift post-starburst galaxies that are likely to be formed through dissipative collapse of gas and rapid star formation prior to quenching (Almaini et al. 2017; Maltby et al. 2018), consistently with our findings.

5 SUMMARY

In this work, we presented a characterization of the molecular gas properties and molecular gas content of galaxies as a function of the compactness of the molecular gas reservoir by using ALMA observations of several CO and [C I] transitions for a sample of 82 far-infrared selected galaxies at $z \sim 1.3$ in COSMOS. We measured the compactness of the molecular gas reservoir by comparing measurements of the molecular gas size to the optical $M_\star$–Size relation for discs at $z \sim 1.25$. We then investigated the relation between the molecular gas properties, the offset from the main sequence and the submillimetre compactness. We further measured molecular gas masses from multiple molecular gas tracers to gain insights on the origin of submillimetre compact galaxies within the main sequence. The main findings of this paper are as follows:

(i) The $\gtrsim$46 per cent of galaxies in our sample have a molecular gas reservoir more compact than the stellar size of typical massive star-forming galaxies at $z \sim 1.3$. The effective radius of the molecular gas reservoir in these sources is on average $\geq 3.3\times$ smaller than their K_s-band effective radius. The compactness of the molecular gas reservoir shows no significant correlation with the main sequence position

(ii) Submillimetre compact galaxies have enhanced CO(5-4)/CO(2-1) and reduced CO(2-1)/$L_{IR,SF}$ luminosity ratios with respect to submillimetre extended galaxies, implying enhanced CO excitation and star formation efficiencies. A significant number of these sources are located within the scatter of the main sequence, blurring the correlation between these ratios and the main sequence offset reported in our previous analysis. Both the CO(5-4)/CO(2-1) and CO(2-1)/$L_{IR,SF}$ luminosity ratios correlate with the submillimetre compactness.

(iii) The average CO SLED of submillimetre compact galaxies up to CO(7-6) is consistent with that of the most extreme main sequence outliers at $z \sim 1.3$. On the other hand, galaxies with an extended molecular gas reservoir have a less excited average CO SLED. This mirrors results from individual line ratios and suggest that the submillimetre compactness provides a good indicator for the CO excitation conditions of a galaxy. Furthermore, this stresses the fact that high-J CO transitions should not be used to derive total molecular gas masses without prior knowledge of the excitation conditions of a galaxy since large variations of the CO excitation are observed within the main sequence itself.

(iv) We find that submillimetre extended and compact galaxies occupy distinct regions in the integrated Schmidt–Kennicutt plane and, in particular, submillimetre compact galaxies have enhanced $L_{IR,SF}$ for a given CO(2-1) luminosity (Fig. 8) indicating enhanced star formation efficiencies similar to starbursts (Fig. 15). A higher star formation efficiency for the submillimetre compact population is also indicated by the intensity of the radiation field, inferred from the far-infrared spectral energy distribution.

(v) We find that submillimetre compact galaxies have higher SFR surface density than extended sources, similar to local starburst galaxies and high-redshift SMGs. We find indications that submillimetre extended galaxies have higher dust temperatures than extended sources, although the average dust temperatures are consistent within the error bars.

(vi) We find that submillimetre compact galaxies within the main sequence are underluminous in CO(2-1) with respect to submillimetre extended main sequence galaxies and off-main sequence sources with similar stellar mass (Fig. 13) and SFR (Fig. 14). Using both the CO(2-1) luminosity and the dust mass as molecular gas tracers, and using α_{CO} and δ_{GDR} conversion factors tailored to the ISM conditions of our sources, we find that the gas fraction mildly increases as a function of the main sequence offset, in qualitative agreement with published scaling relations. However, we find that submillimetre compact galaxies within the main sequence have reduced gas fractions on average, but with a large scatter. While the magnitude of this offset depends on the α_{CO} and δ_{GDR} prescriptions, these results suggest that submillimetre compact galaxies within the main sequence have lower gas fractions with respect to their extended main-sequence counterparts.

Overall, this study shows that the structural properties of galaxies at long wavelengths are a crucial ingredient for interpreting the main sequence of star-forming galaxies at $z \sim 1$. While currently limited to $M_\star \geq 10^{11}\,M_\odot$ where our selection allows us to fully probe the main sequence scatter, our analysis suggests that the compactness of the molecular gas reservoir allows to identify sources with a highly excited, starbursting ISM. Similar to the star formation rate surface density, this parameter provides a good proxy for the ISM conditions of a galaxy while also allowing to rescale for its individual structural properties showing a dependence on the stellar mass. Future crucial steps for our understanding of star formation in distant galaxies will include to perform studies of the molecular gas properties in $M_\star$-selected samples of galaxies with lower stellar masses, to understand if these results also apply to the full main sequence population. Another critical aspect to understand the properties of star-forming galaxies on and above the main sequence at high-z will be to study large galaxy samples at high spatial resolution in the far-infrared/submillimetre regime, where spatially resolved studies have not yet reached the statistics of spatially resolved optical surveys (e.g. Förster Schreiber et al. 2009; Stott et al. 2016). This study has also allowed us to shed light on the origin of submillimetre compact galaxies within the main sequence which are now commonly detected in submillimetre/radio surveys at $z \geq 1$. We argue that their high CO excitation and star formation efficiency, and reduced gas fractions suggest that these sources are associated with an evolutionary phase of the merger. In particular, these properties are consistent with sources in an 'early post-starburst' phase in which the star formation rate has declined and the gas fraction has been reduced as a result of efficient gas consumption while the galaxy retains enhanced excitation and efficiency. Future studies of this population will be crucial for our understanding of passive galaxies formation.

ACKNOWLEDGEMENTS

We would like to thank the referee for their constructive report which significantly improved the content and clarity of the paper. AP acknowledges funding from Region Île-de-France and Incoming CEA fellowship from the CEA-Enhanced Eurotalents program, co-funded by FP7 Marie-Sklodowska-Curie COFUND program (Grant Agreement 600382). AP also gratefully acknowledges financial support from STFC through grants ST/T000244/1 and ST/P000541/1. MTS acknowledges support from a Scientific Exchanges visitor fellowship (IZSEZO 202357) from the Swiss National Science Foundation. AP thanks Ivan Delvecchio and Ian Smail for helpful discussions.

DATA AVAILABILITY

The data used in this paper are available through the ALMA data archive.

REFERENCES

Accurso G. et al., 2017, MNRAS, 470, 4750
Almaini O. et al., 2017, MNRAS, 472, 1401
Ao Y. et al., 2013, A&A, 550, A135
Aravena M. et al., 2019, ApJ, 882, 136
Barro G. et al., 2013, ApJ, 765, 104
Barro G. et al., 2014, ApJ, 791, 52
Barro G. et al., 2016, ApJ, 827, L32
Bayet E., Gerin M., Phillips T. G., Contursi A., 2009, MNRAS, 399, 264
Belli S., Newman A. B., Ellis R. S., 2019, ApJ, 874, 17
Béthermin M. et al., 2015, A&A, 573, A113
Birkin J. E. et al., 2021, MNRAS, 501, 3926
Bolatto A. D., Wolfire M., Leroy A. K., 2013, ARA&A, 51, 207
Boogaard L. A. et al., 2020, ApJ, 902, 109
Bothwell M. S. et al., 2013, MNRAS, 429, 3047
Bournaud F., Daddi E., Weiß A., Renaud F., Mastropietro C., Teyssier R., 2015, A&A, 575, A56
Brusa M. et al., 2018, A&A, 612, A29
Burnham A. D. et al., 2021, ApJ, 910, 89
Cañameras R. et al., 2018, A&A, 620, A61
Carilli C. L., Walter F., 2013, ARA&A, 51, 105
Cassata P. et al., 2020, ApJ, 891, 83
Chabanier S. et al., 2020, A&A, 643, L8
Chabrier G., 2003, PASP, 115, 763
Chen C.-C. et al., 2020, A&A, 635, A119
Cibinel A. et al., 2019, MNRAS, 485, 5631
Circosta C. et al., 2018, A&A, 620, A82
Combes F., García-Burillo S., Braine J., Schinnerer E., Walter F., Colina L., 2013, A&A, 550, A41
Coogan R. T. et al., 2018, MNRAS, 479, 703
Cortzen I. et al., 2020, A&A, 634, L14
Curran S. J., Polatidis A. G., Aalto S., Booth R. S., 2001, A&A, 368, 824
D'Eugenio C. et al., 2020, ApJ, 892, L2
Daddi E. et al., 2010a, ApJ, 713, 686
Daddi E. et al., 2010b, ApJ, 714, L118
Daddi E. et al., 2015, A&A, 577, A46
Daddi E. et al., 2007, ApJ, 670, 156
Dahmen G., Huttemeister S., Wilson T. L., Mauersberger R., 1998, A&A, 331, 959
Dannerbauer H., Daddi E., Riechers D. A., Walter F., Carilli C. L., Dickinson M., Elbaz D., Morrison G. E., 2009, ApJ, 698, L178
Dekel A., Birnboim Y., 2006, MNRAS, 368, 2
Downes D., Solomon P. M., 1998, ApJ, 507, 615
Draine B. T., Li A., 2007, ApJ, 657, 810
Elbaz D. et al., 2018, A&A, 616, A110
Elbaz D. et al., 2007, A&A, 468, 33
Faisst A. L., Carollo C. M., Capak P. L., Tacchella S., Renzini A., Ilbert O., McCracken H. J., Scoville N. Z., 2017, ApJ, 839, 71
Feldmann R., 2020, Commun. Phys., 3, 226
Förster Schreiber N. M. et al., 2009, ApJ, 706, 1364
Franco M. et al., 2020, A&A, 643, A30
Genzel R. et al., 2015, ApJ, 800, 20
Goldreich P., Kwan J., 1974, ApJ, 191, 93
Gómez-Guijarro C. et al., 2019, ApJ, 886, 88
Gómez-Guijarro C. et al., 2021, preprint (arXiv:2106.13246)
Greve T. R. et al., 2005, MNRAS, 359, 1165
Greve T. R. et al., 2014, ApJ, 794, 142
Hodge J. A. et al., 2016, ApJ, 833, 103
Hodge J. A. et al., 2019, ApJ, 876, 130
Hodge J. A., da Cunha E., 2020, R. Soc. Open Sci., 7, 200556
Hodge J. A., Carilli C. L., Walter F., Daddi E., Riechers D., 2013, ApJ, 776, 22

Hung C.-L. et al., 2013, ApJ, 778, 129
Ikarashi S. et al., 2015, ApJ, 810, 133
Jiménez-Andrade E. F. et al., 2019, A&A, 625, A114
Jiménez-Andrade E. F. et al., 2021, ApJ, 910, 106
Jin S. et al., 2018, ApJ, 864, 56
Jin S. et al., 2019, ApJ, 887, 144
Kaasinen M. et al., 2020, ApJ, 899, 37
Kamenetzky J., Rangwala N., Glenn J., Maloney P. R., Conley A., 2014, ApJ, 795, 174
Kamenetzky J., Rangwala N., Glenn J., 2017, MNRAS, 471, 2917
Kaplan E. L., Meier P., 1958, J. Am. Stat. Assoc., 53, 457
Kartaltepe J. S. et al., 2012, ApJ, 757, 23
Kashino D. et al., 2013, ApJ, 777, L8
Kelly B. C., 2007, ApJ, 665, 1489
Kennicutt R. C., 1998, ARA&A, 36, 189
Kirkpatrick A., Sharon C., Keller E., Pope A., 2019, ApJ, 879, 41
Kokorev V. et al., 2021, ApJ, in press
Laigle C. et al., 2016, ApJS, 224, 24
Lamperti I. et al., 2021, preprint (arXiv:2109.02674)
Leroy A. K. et al., 2011, ApJ, 737, 12
Liu D. et al., 2019, ApJS, 244, 40
Liu D. et al., 2021, ApJ, 909, 56
Liu L., Gao Y., Greve T. R., 2015a, ApJ, 805, 31
Liu D., Gao Y., Isaak K., Daddi E., Yang C., Lu N., van der Werf P., 2015b, ApJ, 810, L14
Magdis G. E. et al., 2012, ApJ, 760, 6
Magdis G. E. et al., 2017, A&A, 603, A93
Magnelli B. et al., 2012, A&A, 548, A22
Maltby D. T., Almaini O., Wild V., Hatch N. A., Hartley W. G., Simpson C., Rowlands K., Socolovsky M., 2018, MNRAS, 480, 381
Mancini C. et al., 2019, MNRAS, 489, 1265
Mannucci F., Cresci G., Maiolino R., Marconi A., Gnerucci A., 2010, MNRAS, 408, 2115
McCracken H. J. et al., 2012, A&A, 544, A156
Mihos J. C., Hernquist L., 1996, ApJ, 464, 641
Mullaney J. R., Alexander D. M., Goulding A. D., Hickox R. C., 2011, MNRAS, 414, 1082
Narayanan D., Krumholz M. R., 2014, MNRAS, 442, 1411
Narayanan D., Krumholz M. R., Ostriker E. C., Hernquist L., 2012, MNRAS, 421, 3127
Nelson E. J. et al., 2012, ApJ, 747, L28
Nelson E. et al., 2014, Nature, 513, 394
Nelson E. J. et al., 2016, ApJ, 828, 27
Noeske K. G. et al., 2007, ApJ, 660, L43
Pannella M. et al., 2015, ApJ, 807, 141
Papadopoulos P. P., Thi W. F., Viti S., 2004, MNRAS, 351, 147
Papadopoulos P. P., van der Werf P. P., Xilouris E. M., Isaak K. G., Gao Y., Mühle S., 2012, MNRAS, 426, 2601
Peng C. Y., Ho L. C., Impey C. D., Rix H.-W., 2010, AJ, 139, 2097
Pettini M., Pagel B. E. J., 2004, MNRAS, 348, L59
Popping G. et al., 2017, A&A, 602, A11
Popping G. et al., 2021, preprint (arXiv:2101.12218)
Puglisi A. et al., 2017, ApJ, 838, L18
Puglisi A. et al., 2019, ApJ, 877, L23
Puglisi A. et al., 2021, Nat. Astron., 5, 319
Rangwala N. et al., 2011, ApJ, 743, 94
Renzini A., Peng Y.-J., 2015, ApJ, 801, L29
Riechers D. A., Hodge J., Walter F., Carilli C. L., Bertoldi F., 2011, ApJ, 739, L31
Rodighiero G. et al., 2011, ApJ, 739, L40
Rodighiero G. et al., 2014, MNRAS, 443, 19
Sargent M. T. et al., 2014, ApJ, 793, 19
Sargent M. T., Béthermin M., Daddi E., Elbaz D., 2012, ApJ, 747, L31
Scholtz J. et al., 2020, MNRAS, 492, 3194
Schreiber C. et al., 2015, A&A, 575, A74
Scoville N. et al., 2007, ApJS, 172, 1
Scoville N. et al., 2014, ApJ, 783, 84
Scoville N. et al., 2016, ApJ, 820, 83
Silverman J. D. et al., 2015a, ApJS, 220, 12
Silverman J. D. et al., 2015b, ApJ, 812, L23
Silverman J. D. et al., 2018a, ApJ, 867, 92
Silverman J. D. et al., 2018b, ApJ, 868, 75
Simpson J. M. et al., 2017, ApJ, 839, 58
Solomon P. M., Vanden Bout P. A., 2005, ARA&A, 43, 677
Solomon P. M., Rivolo A. R., Barrett J., Yahil A., 1987, ApJ, 319, 730
Speagle J. S., Steinhardt C. L., Capak P. L., Silverman J. D., 2014, ApJS, 214, 15
Springel V., Hernquist L., 2005, ApJ, 622, L9
Stott J. P. et al., 2016, MNRAS, 457, 1888
Tacchella S., Dekel A., Carollo C. M., Ceverino D., DeGraf C., Lapiner S., Mand elker N., Primack Joel R., 2016, MNRAS, 457, 2790
Tacconi L. J. et al., 2018, ApJ, 853, 22
Tacconi L. J., Genzel R., Sternberg A., 2020, ARA&A, 58, 157
Tadaki K.-I. et al., 2017a, ApJ, 834, 135
Tadaki K.-I. et al., 2017b, ApJ, 841, L25
Tadaki K.-I. et al., 2020, ApJ, 901, 74
Talia M. et al., 2018, MNRAS, 476, 3956
Tan Q. et al., 2014, A&A, 569, A98
Valentino F. et al., 2018, ApJ, 869, 27
Valentino F. et al., 2020, A&A, 641, A155
Valentino F. et al., 2021, preprint (arXiv:2109.03842)
van der Tak F. F. S., Black J. H., Schöier F. L., Jansen D. J., van Dishoeck E. F., 2007, A&A, 468, 627
van der Wel A. et al., 2014, ApJ, 788, 28
van der Werf P. P. et al., 2010, A&A, 518, L42
van Dokkum P. G. et al., 2015, ApJ, 813, 23
Weiß A., Neininger N., Hüttemeister S., Klein U., 2001, A&A, 365, 571
Weiß A., Henkel C., Downes D., Walter F., 2003, A&A, 409, L41
Weiß A., Walter F., Scoville N. Z., 2005, A&A, 438, 533
Weiß A., Downes D., Neri R., Walter F., Henkel C., Wilner D. J., Wagg J., Wiklind T., 2007, A&A, 467, 955
Whitaker K. E. et al., 2014, ApJ, 795, 104
Wuyts S., Förster Schreiber N. M., Lutz D. et al., 2011, ApJ, 738, 106
Yang C. et al., 2017, A&A, 608, A144
Zhang Z.-Y. et al., 2014, A&A, 568, A122
Zolotov A. et al., 2015, MNRAS, 450, 2327

APPENDIX A: EXPLORING THE DEPENDENCE OF μ_{GAS} OF MAIN-SEQUENCE GALAXIES ON α_{CO} AND δ_{GDR}

In this appendix, we explore the dependence of the results presented in Section 3.4 and Fig. 16 on the choice of the observable-to-gas conversion factor. The main goal of this test is to explore the difference in gas fraction between extended and compact galaxies on the main sequence, since this aspect is critical for our interpretation of the submillimetre compact population within the main sequence (see Section 4). To quantify the dependence of our results on the observable-to-gas conversion factors, we compute gas fractions for galaxies on the main sequence by adopting metallicity-dependent α_{CO} and δ_{GDR} conversion factors, following the prescription of Magdis et al. (2012). The metallicity of our galaxies is $8.43 \leq Z \leq 8.78$ with a median value of $Z = 8.71$, as derived from the fundamental mass–metallicity relation of Mannucci et al. (2010) (FMR) considering a Pettini & Pagel (2004) metallicity scale.

In the top row of Fig. A1, we show the gas fraction from $L'_{CO(2-1)}$ when adopting a metallicity-dependent α_{CO} for galaxies within the main sequence. We find median gas fractions of $\mu_{gas,\,Compacts,\,MS} = 0.46 \pm 0.20$ and $\mu_{gas,\,Extended,\,MS} = 0.83 \pm 0.27$. In the bottom row of Fig. A1, we show the gas fractions from M_{dust} by adopting a δ_{GDR} that varies as a function of the metallicity for galaxies within the main sequence. We find median gas fractions of $\mu_{gas,\,Compacts,\,MS} = 0.13 \pm 0.10$ and $\mu_{gas,\,Extended,\,MS} = 0.26 \pm 0.16$. Finally, using a

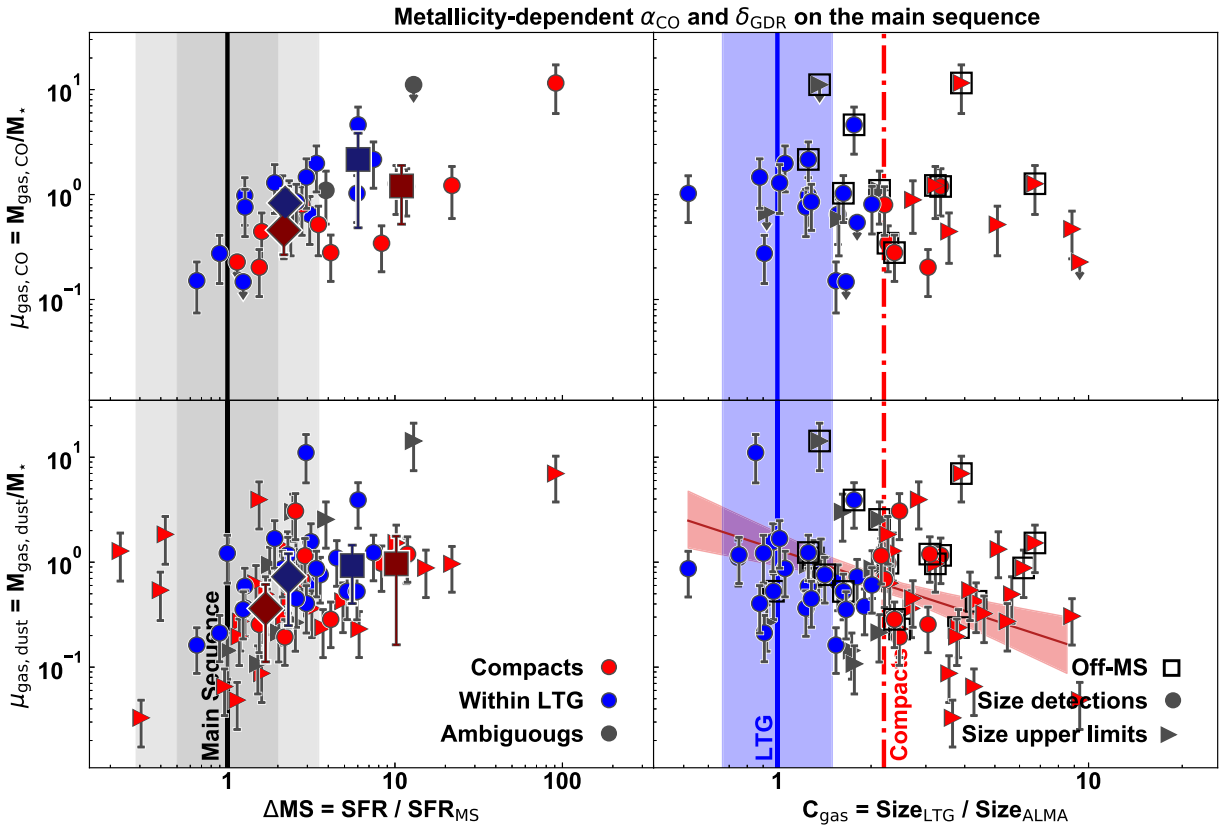

Figure A1. As Fig. 16 but using metallicity-dependent α_{CO} and δ_{GDR} conversion factors for galaxies on the main sequence. We consider constant conversion factors for galaxies above the main sequence, as in the main text.

metallicity-dependent δ_{GDR} provides a slope, normalization, and intrinsic scatter for the C_{gas}–$\mu_{gas,\,dust}$ relation that is consistent within the error bars to that reported in Table 2 while providing a lower correlation index ($\rho = -0.3$). This figure shows that compact main sequence galaxies show a reduced gas fraction, on average, although considering the metallicity dependence of the α_{CO} and δ_{GDR} reduces the difference with respect to the extended population. We summarize our results for the average gas fractions measured for galaxies on and above the main sequence with different tracers and observable-to-gas conversion factors prescriptions in Table A1.

Finally, in Fig. A2 we show the comparison between M_{gas} computed from $L'_{CO(2-1)}$ and M_{dust}, using the α_{CO} and δ_{GDR} specified in the caption. This figure shows a very good agreement between CO-based and dust-based gas masses for the compact galaxies, supporting our choice of starburst-like conversion factors for this class of objects. At the same time, this figure suggests that the gas mass of a subset of extended galaxies might be overestimated (underestimated) by a factor of ∼0.25 dex when adopting $\alpha_{CO} = 3.6$ ($\delta_{GDR} = 85$). This does not substantially affect our conclusions.

The small discrepancy in the gas masses measured from $L'_{CO(2-1)}$ and M_{dust} might suggests variation in the $L'_{CO(2-1)}/M_{dust}$ ratio as a function of the main sequence offset and/or compactness. In Fig. A3, we thus investigate for the presence of variations in the $L'_{CO(2-1)}/M_{dust}$ ratio as a function of the main sequence offset and of the compactness for galaxies with detections or reliable $L'_{CO(2-1)}$ upper limits and robust measurements of M_{dust}. This plot shows that there is no clear dependence of the $L'_{CO(2-1)}/M_{dust}$ ratio on the main sequence offset nor the compactness. The median $L'_{CO(2-1)}/M_{dust}$ ratio for compact and extended galaxies on and above the main sequence is consistent within the error bars. This suggests that CO and dust give equivalent results in terms of the molecular gas mass of compact and extended galaxies, without introducing biases.

Table A1. Average gas fractions for extended and compact galaxies across the main sequence using different observable-to-gas conversion factors.

Method	$\mu^{(a)}_{\rm gas,Extended,MS}$	$\mu^{(a)}_{\rm gas,Compacts,MS}$	$\mu^{(b)}_{\rm gas,Extended,off-MS}$	$\mu^{(b)}_{\rm gas,Compacts,off-MS}$
Bimodal $\alpha_{\rm CO}$ - Compactness	1.04 ± 0.34	0.12 ± 0.05	2.2 ± 1.7	1.14 ± 0.7
$\alpha_{\rm CO}$(Z)	0.83 ± 0.27	0.46 ± 0.20	--	–
Bimodal $\delta_{\rm GDR}$ - Compactness	0.66 ± 0.34	0.12 ± 0.09	0.93 ± 0.52	0.97 ± 0.80
$\delta_{\rm GRD}$(Z)	0.73 ± 0.48	0.36 ± 0.25	–	–

Notes.[(a)] $1 \leqslant \Delta$MS<3.5
[(b)] ΔMS≥ 3.5

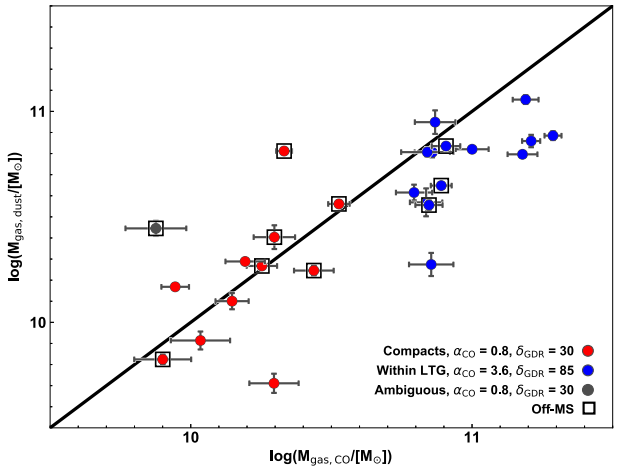

Figure A2. Comparison of the gas mass from $M_{\rm dust}$ [$M_\odot$] and from $L'_{\rm CO(2-1)}$ [K km s^{-1} pc^2] for the galaxies with a robust dust mass estimate and a secure CO(2-1) detection. The solid line is the 1:1 relation.

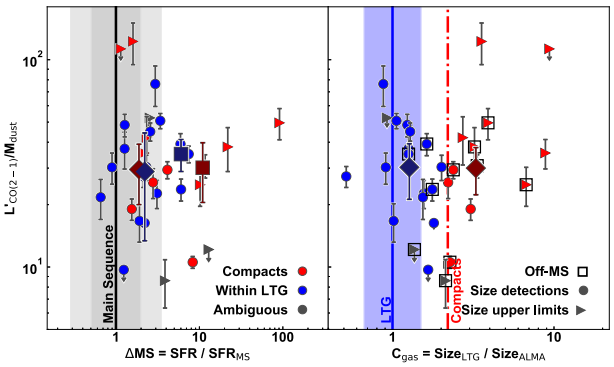

Figure A3. The $L'_{\rm CO(2-1)}/M_{\rm dust}$ ratio as a function of the main sequence offset (left-hand panel) and of the compactness (right-hand panel) for galaxies with detections or reliable $L'_{\rm CO(2-1)}$ upper limits and robust measurements of $M_{\rm dust}$. In the left-hand panel, large filled diamonds and large filled squares show the median $L'_{\rm CO(2-1)}/M_{\rm dust}$ ratio for compact and extended galaxies on and above the main sequence, respectively. Large filled diamonds in the right-hand panel show the median $L'_{\rm CO(2-1)}/M_{\rm dust}$ ratio for extended and compact galaxies. The errors on the average measurements are the interquartile range of the $L'_{\rm CO(2-1)}/M_{\rm dust}$ distribution.

This paper has been typeset from a TEX/LATEX file prepared by the author.